Article:

Green, D., Nippress, S., Nowacki, A. orcid.org/0000-0001-7669-7383 et al. (9 more authors) (Accepted: 2025) Seismic Waves Generated by Explosions In, and Above, Saturated Sediments: The Foulness Seismoacoustic Coupling Trials. Geophysical Journal International. ISSN 0956-540X (In Press)

Seismic Waves Generated by Explosions In, and Above, Saturated Sediments: The Foulness Seismoacoustic Coupling Trials

Journal:	*Geophysical Journal International*
Manuscript ID	GJI-25-0027.R2
Manuscript Type:	Research Paper
Date Submitted by the Author:	12-May-2025

Complete List of Authors:	Green, David; AWE Blacknest, Forensic Seismology Nippress, Stuart; Atomic Weapons Establishment, Blacknest Nowacki, Andy; University of Leeds, School of Earth and Environment Clark, Roger; University of Leeds, School of Earth and Environment Read, Evie; University of Bristol, Department of Earth Sciences Can Postaci, Tugce; University of Leeds, School of Earth and Environment Tilbury, Chris; Spurpark Ltd. Benson, Nick; University of Bristol, Department of Earth Sciences de Ridder, Sjoerd; University of Leeds, School of Earth and Environment Wookey, James; University of Bristol, Department of Earth Sciences Teanby, N.; University of Bristol, Department of Earth Sciences Stone, Barry; Spurpark Ltd.

Keywords:	Controlled source seismology < SEISMOLOGY, Earthquake monitoring and test-ban treaty verification < SEISMOLOGY, Wave propagation < SEISMOLOGY

Note: The following files were submitted by the author for peer review, but cannot be converted to PDF. You must view these files (e.g. movies) online.
FSCT_displacement_measurements.csv.gz

Seismic Waves Generated by Explosions In, and Above, Saturated Sediments: The Foulness Seismoacoustic Coupling Trials

David N. Green[1], Stuart E. J. Nippress[1], Andy Nowacki[2], Roger A. Clark[2], Evie Read[3], Tuğçe Can Postacı[2,†], Chris Tilbury[4], Nick Benson[3], Sjoerd A. L. de Ridder[2], James Wookey[3], Nicholas A. Teanby[3], Barry Stone[4]

1. AWE Blacknest, Brimpton, Reading, UK
2. School of Earth and Environment, University of Leeds, Woodhouse Lane, Leeds, UK
3. Department of Earth Sciences, University of Bristol, Wills Memorial Building, Queens Road, Bristol, UK
4. Spurpark Ltd., Shoeburyness, Essex

†Now at General Directorate of Mineral Research and Exploration, Department of Geophysical Studies, Ankara, Turkey

Address for correspondence

Dr. D. N. Green

AWE Blacknest

Brimpton

Reading

RG7 4RS

United Kingdom

dgreen@blacknest.gov.uk

Summary

Seismic signals generated by near-surface explosions, with sources including industrial accidents and terrorism, are often analysed to assist post-detonation forensic characterisation efforts such as estimating explosive yield. Explosively generated seismic displacements are a function of, amongst other factors: the source-to-receiver distance, the explosive yield, the height-of-burst or depth-of-burial of the source and the geological material at the detonation site. Recent experiments in the United States, focusing on ground motion recordings at distances of $<$15 km from explosive trials, have resulted in empirical models for predicting *P*-wave displacements generated by explosions in and above hard rock (granite, limestone), dry alluvium, and water. To extend these models to include sources within and above saturated sediments we conducted eight explosions at Foulness, Essex, UK, where $\sim$150 m thicknesses of alluvium and clay overlie chalk. These shots, named the Foulness Seismoacoustic Coupling Trials (FSCT), had charge masses of 10 and 100 kg TNT equivalent and were emplaced between 2.3 m below and 1.4 m above the ground surface. Initial *P*-wave displacements, recorded between 150 and 7000 m from the explosions, exhibit amplitude variations as a function of distance that depart from a single power-law decay relationship. The layered geology at Foulness causes the propagation path that generates the initial *P*-wave to change as the distance from the source increases, with each path exhibiting different amplitude decay rates as a function of distance. At distances up to 300 m from the source the first arrival is associated with direct propagation through the upper sediments, while beyond 1000 m the initial *P*-waves are refracted returns from deeper structure. At intermediate distances constructive interference occurs between *P*-waves propagating through the upper sediments and those returning from velocity-depth gradients at depths between 100 and 300 m. This generates an increase in displacement amplitude, with a maximum at $\sim$800 m from the source. Numerical waveform modelling indicates that observations of the amplitude variations is in part the consequence of high *P*- to *S*-wave velocity ratios within the upper 150 m of saturated sediment, resulting in temporal separation of the *P*- and *S*-arrivals. We extend a recently developed empirical model formulation to allow for such distance-dependent amplitude variations. Changes in explosive height-of-burst within and above the saturated sediments at Foulness result in large *P*-wave amplitude variations. FSCT surface explosions exhibit *P*-wave displacement amplitudes that are a factor of 22 smaller than coupled explosions at depth, compared to factors of 2.3 and 7.6 reported for dry alluvium and granite respectively.

Keywords:
Controlled source seismology
Earthquake monitoring and test-ban treaty verification
Wave propagation

1 Introduction

Recordings of explosively generated seismic waves can be used to estimate the yield (or charge mass) of a detonation. Historically, significant effort has been expended in identifying relationships between seismic signal parameters, including amplitudes and associated magnitude estimates, and the yield of underground nuclear test explosions (e.g., Douglas and Marshall, 1996).

As seismometer deployments have become more widespread, recordings from smaller conventional explosive sources have become more commonplace. Unlike underground nuclear tests these sources are often close to the surface. Examples include truck bomb detonations (Koper et al., 1999, 2002), accidental industrial explosions (Pilger et al., 2021; Song et al., 2022), and munition storage accidents (Nippress et al., 2023). To estimate an explosive yield for such sources, the analyst must account for the partitioning of kinetic explosive energy into seismic waves, damage (e.g., crater formation) and airborne acoustics.

Near-surface explosions generate smaller seismic signals than fully coupled buried explosions with commensurate charge masses (e.g., Khalturin et al., 1998). Over the past decade there has been a concerted effort to design, and execute, experiments that allow the variation in seismic coupling as a function of explosive height-of-burst or depth-of-burial to be determined (e.g., Bonner et al., 2013a,b). The results have allowed empirical models for seismic displacement to be constructed (e.g., Ford et al., 2014, 2021; Templeton et al., 2018) and then validated against other datasets (e.g., Pasyanos and Ford, 2015; Kim and Pasyanos, 2023).

For simplicity, we describe height-of-burst and depth-of-burial variations by one continuous parameter, which we denote HoB, with negative/positive values indicating subsurface/subaerial explosions (following the notation of Templeton et al., 2018).

Empirical models for predicting explosively generated initial P-wave seismic displacements must account for variations caused by: the distance from the source at which the recording is made, the explosive yield, the explosion HoB, and the geological setting in which the explosion and seismic propagation takes place (e.g., Ford et al., 2014, 2021). The dependence on geological setting limits the wider applicability, or transportability, of such empirical models. In addition, simplifications such as the assumption of isotropic seismic source radiation are often implicit within the model formulation. When interpreting signals generated by an explosion in a given location, an analyst has to consider the applicability of models validated using trials data collected at a different site.

The field trials data from which the empirical models were built have also illustrated the benefit of multi-parameter recordings. With measurements of a single phenomenon (e.g., seismic body waves) it is difficult to distinguish between the effects of variations in HoB and yield. The joint analysis of seismic and airborne acoustic (blast) data has been successful in resolving this parameter trade-off (Ford et al., 2014; Williams et al., 2021).

Ford et al. (2021) report seismic displacement models for three generic rock-type environments: hard (granite, limestone), soft (alluvium, soil) and wet (saturated soil). Little information is given regarding the geological variations as a function of depth at the trial locations, and the specific propagation paths taken by the initial *P*-wave as a function of source-to-receiver distance are not considered. These factors are unimportant in areas of homogeneous geology, where the initial *P*-wave will, at all relevant distances, be a direct wave within the same material as that in which the explosion was detonated. The assumption of direct *P*-wave paths is attractive because signal amplitude decay as a function of distance may be explained by a simple power-law relationship. However, in layered geologies (for example, where sediments overlie bedrock), variations in the path taken by the initial *P*-wave (direct wave, refracted head wave) lead to more complex variations in initial *P*-wave amplitude with distance (e.g., Červený, 1966; Banda et al., 1982). Therefore, it is important to understand the applicability of empirical seismic displacement models, such as those of Ford et al. (2014, 2021), in environments where the initial *P*-wave path changes as a function of distance.

Additionally, the Ford et al. (2021) wet-rock model is only constrained by data from the Humming Terrapin trials series, for which the majority of the explosions occurred within or above large ponds at Aberdeen Proving Ground, Maryland, US (Stone, 2017). Therefore, questions remain about whether the Ford et al. (2021) wet-rock model is applicable to explosions in and above saturated sediment, or whether it should only be used for detonations in and above water.

A series of eight explosions were conducted to address the gap in knowledge regarding *P*-wave amplitude variation, as a function of HoB, for explosions in and above saturated sediment. The trials, conducted on Foulness Island, Essex, UK, and referred to as the Foulness Seismoacoustic Coupling Trials (abbreviated to FSCT) were undertaken within and above saturated alluvium and clays overlying more competent sedimentary rocks (Sections 2 & 3).

In this paper we have focused upon ground motion recordings at distances of between 20 and 7000 m from the explosions (Section 4). These measurements have increased our understanding of energy partitioning for sources within, and above, soft saturated sediments, and allow comparison to previous results. We utilized numerical modelling to improve our understanding of the initial *P*-wave travel time and amplitude measurements (Section 5). In particular, the modelling results suggest that observed distance-dependent variations in signal amplitude decay rates can be attributed to the effect of geological layering beneath Foulness Island. These findings have been incorporated into a seismic displacement model (Section 6), based upon that of Ford et al. (2021).

2 Foulness Seismoacoustic Coupling Trials

FSCT comprised eight detonations within a 75 m $\times$ 75 m area of undisturbed ground (referred to as the shotpad) at a UK Ministry of Defence firing range on Foulness Island, Essex, UK, during October 2021 (Fig. 1, Table 1). The site was chosen due to the >100 m underlying thicknesses of alluvium and clays, facilitating a HoB experiment in soft saturated sediments. A pre-FSCT reflection and refraction seismic survey was conducted to understand the seismic velocity structure in the vicinity of the shotpad (Collins, 2018), and a detailed geological description is provided in Section 3.

The eight explosive charges, referred to as S1 to S8, had equivalent TNT charge masses of 10 kg (S1,S7,S8) and 100 kg (S2 to S6) and were constructed as cylinders to allow emplacement within boreholes. The aspect ratio of the cylinder (1:1.57) was a compromise between requiring a compact source and ensuring a tight fit within the boreholes. The lateral spacing between the explosions across the shotpad (Fig. 1c) was designed to minimize interaction between the explosively generated craters. The allowable FSCT charge mass was restricted by Foulness site regulations, such that the shots were smaller than the explosions underpinning previous empirical models; the distribution of explosive charge masses used in the Ford et al. (2021) analysis had a lower quartile to upper quartile range of 91 to 540 kg.

The explosive package centroid depths were between 2.32 m below the ground surface (S2) and a height of 1.36 m above the ground surface (S6) (Fig. 1d). The above-ground charge (S6) was placed on a wooden platform, and the on-surface explosives (S5,S7,S8) were placed on a thin cardboard sheet. The below-ground explosives (S1 to S4) were emplaced at the base of boreholes, lined using a single length of ribbed high-density polyethylene (HDPE) pipe that ensured the surrounding alluvial sediments did not collapse before charge emplacement. Any small gap ($<$100 mm) between the HDPE liner and the edge of the drilled hole was backfilled with sharp sand. Once the charge and cabling were securely deployed at the base of the borehole, sharp sand was used to stem the borehole to surface level taking care to ensure no voids were present around the charge casing. Further details of the explosives and their emplacement are given in Supplementary Material Section A.

An instrumentation suite was deployed across Foulness Island (Fig. 1 and Table 2) to record the seismoacoustic wavefield generated by the FSCT explosions. This paper focuses on seismic data collected at distances of 150 to 7000 m (37 to 1500 m/kg$^{1/3}$ from the 100 kg explosions) for comparison with the models of Ford et al. (2014, 2021) alongside closer proximity (<100 m) accelerometer data that allows comparison with ground shock studies (e.g., Drake and Little, 1983). Continuous seismic data, collected across ~1 month, is available (Green and Nowacki, 2021), although not analysed in depth here. Blast wave data, collected on piezoelectric sensors, did not capture the whole low-frequency waveform leading to impulse measurements being underpredicted; an issue identified by Ford et al. (2014). However, recorded peak pressures for the above ground shots were consistent with the blast wave model of Kinney and Graham (1985), and the reduction in peak pressure for buried explosions agrees with the observations of Ford and Vorobiev (2023). For completeness this analysis is detailed in Supplementary Material Fig. S1. High-speed video of the explosions and 3D laser scans of the resultant craters were also made but have yet to be comprehensively analysed.

3 Geological Setting

Foulness Island, a ~10×4 km area of reclaimed coastal marshland, is located on the northern shore of the Thames Estuary, ~70 km east of London (Fig. 1a inset). The geological sequence underneath the island can, to first order, be described by a six layer model (progressing downward from the surface): Marine and estuarine alluvium (with a thickness of ~20 m), London Clay (~100 m thickness), Lower London Tertiaries (~40 m thickness), Chalk (~200 m thickness), Upper Greensand and Gault Clay (~40 m thickness) underlain by Palaeozoic Basement Sandstones. The upper 200 m of the sedimentary sequence beneath Foulness Island has been constrained from a small number of historical boreholes (e.g., Figs. 1a and 2a).

The upper ~20 m at Foulness consists of unconsolidated marine and estuarine alluvium deposits, predominantly formed of clays, silts and sands. Previous studies suggest that the alluvial deposits exhibit *P*-wave velocities (v_p) of between 1.5 and 1.9 km/s (Conway et al., 1984). Within 500 m of the FSCT shotpad, borehole logs indicate that the alluvium comprises

~8 m of sand overlain by ~9 m of clays and silts (Boshier, 1982, 1983, and summarised in Fig. 2a). Undrained triaxial compression tests and consolidation tests indicated that the upper two to three metres of material has a bulk density of between 1.6 and 2.0 Mg/m^3. Cohesion (shear strength) values exhibit large variations, but reduce from between 15 and 105 kPa in the desiccated upper layer to between 3 and 10 kPa at depths of 2 to 3 m. This led Boshier (1983) to conclude that the clays at the depths of the deepest FSCT explosions (~2.3 m) should be classified as very soft.

Beneath the upper alluvial layers lies a ~90 m thickness of London Clay, a unit comprised of silty and sandy clays (e.g. Lake et al., 1986); for the purposes of our study we do not attempt to subdivide this into finer lithological units. Across Foulness Island the mapped depth to the base of the London Clay is remarkably consistent, with depths between 103 and 111 m below the surface (Lake et al., 1986, and Fig. 2a). London Clay is likely characterised by high v_p/v_s ratios (>5); mean v_p measurements are ~1.6 km/s, while shear wave velocities (v_s) of between 200 and 300 m/s are reported (e.g., Conway et al., 1984; Hight et al., 1997; Lessi-Cheimariou et al., 2019). Samples of London Clay collected at other UK locations exhibit mechanical anisotropy (e.g., Nishimura et al., 2007), but we are unaware of dedicated studies at Foulness and this property is not considered further in this paper.

Below the London Clay lies a ~40 m thickness of Palaeogene sediments laid down in a mixture of shallow sea, coastal and fluvial environments (e.g., Sumbler, 1996). We refer to these using the historical "Lower London Tertiaries" classification, rather than splitting the layer into the Lambeth Group (upper ~10 m of sands) and Thanet Sand (lower ~30 m of clays and sands) due to the low confidence in being able to distinguish between the two in historical borehole records. Seismic investigations of the Lower London Tertiaries at a site ~85 km to the north-east of Foulness suggests that shear-wave velocities within this unit are low ($v_s < 500$ m/s), with the clays of the Thanet Sand perhaps forming a low-velocity zone with v_s as low as 300 m/s (Hight et al., 1997).

Carboniferous chalk deposits underlie the Lower London Tertiaries (Fig. 2a), with the interface at a depth of ∼160 m (Lake et al., 1986). Although the deposit thickness has not been proven via drilling on Foulness Island, deep boreholes across the Thames Estuary region have revealed a relatively consistent 200±15 m thickness of chalk. Despite southern UK chalk having variable geomechanical strength properties, related in part to the presence of clay-rich marl beds (e.g., Bell et al., 1999), a single layer description is sufficient for our purposes. Beneath the chalk the closest deep borehole, 18 km from the FSCT shotpad, reveals a 40 m thickness of early Cretaceous sandstones and mudstones (the Upper Greensand and Upper Gault) before Palaeozoic sandstones are reached at a depth of ∼400 m (Smart et al., 1964; Lake et al., 1986).

A seismic reflection survey, conducted a few hundred metres to the north-east of the FSCT shotpad (see Collins, 2018; Can, 2020), resulted in a v_p profile (Fig. 2b). This suggests that the sediments in the upper ∼100 m have v_p values of ∼1.7 km/s, with the upper <10 m likely exhibiting lower v_p of ∼1.2 km/s. Below these units, the first-order behaviour is a positive v_p gradient with increasing depth, such that at a depth of ∼400 m the estimated v_p has increased to between 3.5 and 4.0 km/s.

4 Data and Results

The focus of this paper is to understand better the variability in seismic amplitudes generated by near-surface explosions within saturated sediment environments, and the influence of layered geological structures upon the observations. In this section we describe the analysis methodologies applied to, and results gained from, FSCT ground motion data collected on (i) accelerometers at distances <90 m from the explosions and (ii) seismometers located across Foulness Island at distances between 150 and 7000 m from the shotpad.

In studies of explosively generated phenomena, including seismic amplitudes, hydrodynamic scaling relationships are often employed to relate measurements across wide ranges of physical time and length scales (e.g., Ford et al., 2021). These scaling laws describe how, for point-source explosions, time and length scale with the cube-root of yield (e.g., Denny and Johnson, 1991); cube-root scaling has been validated for seismic displacement measurements from near-surface explosions (Templeton et al., 2018). Following the notation of Ford et al. (2021), we denote scaled variables with an over tilde. For example, the physical source-to-receiver distance is given by r (m), while the scaled distance is $\tilde{r} = rW^{-1/3}$ (m/kg$^{1/3}$) where W is the explosive charge mass, or yield.

4.1 Near-Source Acceleration Recordings

Four Endevco Model 2228C triaxial piezoelectric accelerometers, with a flat response ($\leq$5% deviation) to accelerations between 1 and 4000 Hz, were emplaced at a depth of 0.6 m below the ground surface along a radial line approximately North-West from the centre of the explosives pad (Fig. 1c), such that the distances between detonation and sensor varied between 17 m (for the closest sensor to S3) and 87 m (for the furthest sensor from S4). Recordings were made at 1×10^6 samples per second. Prior to deployment the corners of each sensor were screwed onto the top of a metal rod that was then set into a plaster cube with edge lengths of 100 mm; this cube provided a stable base for the sensor with a density similar to that of the surrounding ground material. Across the weeks of deployment the vertical component recordings proved to be more reliable than the horizontal components, some of which failed likely due to water ingress during the experiment. Therefore, only vertical recordings are considered within this analysis.

The acceleration recordings (e.g., Fig. 3) consist of arrivals that have both propagated through the ground to the station and, for explosions at or above the surface, an air-to-ground coupled phase associated with the later arrival of the blast wave (not shown). The FSCT recordings of the ground propagated wave consist of short (<0.05 s) waveforms with a peak frequency content of between 100 and 200 Hz; they do not exhibit the classic rapid onset and exponential decay of ground shock recordings at very short stand-off distances (e.g., Shelton et al., 2014). Across the twenty observations from explosions S1 to S5 the arrival times of the first arrival on the vertical channel is consistent with a propagation velocity of 1.66$\pm$0.06 km/s (median value $\pm$ median absolute deviation).

Previous studies of ground motions close to explosions include the Department of the Army (1986) Technical Manual, referred to here as TM 5-855-1, that builds on work by Drake and Little (1983). To compare Foulness recordings with ground velocity relationships in TM 5-855-1, a linear trend was removed from unfiltered FSCT acceleration recordings prior to integration. The peak particle velocity (PPV) was then measured as the maximum zero-to-peak amplitude on the vertical component recording. PPV values decrease with both distance from the source (Fig. 3a), as expected due to geometric spreading and attenuation, and as the explosive HoB increases. TM 5-855-1 provides empirically-derived relationships for expected PPV values close to explosions within various soil types, which in metric units can be expressed as,

$$V_0(\tilde{r}, \tilde{h}, n) = 48.77 f(\tilde{h})\,(2.5208\tilde{r})^{-n} \tag{1}$$

where V_0 is the peak particle velocity (m/s), $\tilde{r}$ is the scaled source-to-receiver distance (m/kg$^{1/3}$), $\tilde{h}$ is the scaled height-of-burst (m/kg$^{1/3}$), $f(\tilde{h})$ is a ground shock coupling factor, and n is a geologically-dependent coefficient that accounts for geometrical spreading and attenuation. Values of n vary between 1.5 for heavy saturated clays and 3.25 for loose, dry sands.

We fit a TM 5-855-1 model (eq. 1) to the FSCT PPV measurements made within 100 m of the explosions, to confirm they are consistent with previous recordings in, and above, saturated soils. To estimate n for the FSCT data we make the assumption that explosions S1 and S2 are fully coupled, i.e., f=1 (the TM 5-855-1 $f(\tilde{h})$ function indicates $f >$0.95 for the S1 and S2 HoB values). Minimising the sum of squared residuals between the S1 and S2 PPV observations and the eq. 1 predictions, across a physically reasonable range of n values, results in an estimate of n=1.8 (black line, Fig. 3a). This is consistent with previous measurements in saturated sandy clays. However, it is noted that the calculation has limitations including: (1) the original measurements were made at shorter scaled distances (<12 m/kg$^{1/3}$) than we have access to at FSCT, and (2) the fit is sensitive to the limited range of scaled distances at which we observe S1 and S2.

To compare to the HoB coupling curve of TM 5-855-1 (i.e., $f(\tilde{h})$) we normalise the Foulness PPV measurements, $\mathrm{PPV}_{\mathrm{meas}}$, with respect to the predicted value, $\mathrm{PPV}_{\mathrm{pred}}$, for a fully coupled explosion at the measurement distance, taking $n = 1.80$,

$$f_{\mathrm{FSCT}}(\tilde{h}) = \frac{\mathrm{PPV}_{\mathrm{meas}}(\tilde{r},\tilde{h})}{\mathrm{PPV}_{\mathrm{pred}}(\tilde{r},\tilde{h},n)} = \frac{\mathrm{PPV}_{\mathrm{meas}}(\tilde{r},\tilde{h})}{V_0(\tilde{r},-1,1.80)} \tag{2}$$

Once the effect of amplitude decay with distance has been removed, measured PPV values reduce by approximately two orders of magnitude between fully coupled (S1 at $\tilde{h}$=-1.0 m/kg$^{1/3}$) and above ground explosions (S6 at $\tilde{h}$=0.3 m/kg$^{1/3}$). The calculated $f_{\mathrm{FSCT}}(\tilde{h})$ values exhibit a more gradual reduction in PPV as a function of increasing $\tilde{h}$ when compared to the TM 5-855-1 $f(\tilde{h})$ function (Fig. 3b), which reduces rapidly between $\tilde{h}=-0.1$ and $\tilde{h}$=0.1 m/kg$^{1/3}$. However, the coupling for a surface explosion (e.g., S5 where the FSCT coupling factor ∼0.1) is close to that recommended by TM 5-855-1 for contact bursts (f=0.14).

4.2 Ground Velocity Recordings Across Foulness Island

The FSCT seismic network contained 12 broadband sensors and 46 geophones (Fig. 1a); all sensors recorded three orthogonal components of motion. The broadband seismometer network consisted of 10 Güralp Certimus sensors (locations TR01 to TR10) and two Güralp 6TD sensors (locations TR11 and TR12); all broadband sensors recorded at 250 samples per second. These sensors spanned a distance range of [360,6960] m from the centre of the

FSCT shotpad. The broadband sensors were deployed upon a metal plate sitting on a bed of compacted damp sand within a sunken barrel, and timing information was provided by an external Global Navigation Satellite System (GNSS) antenna. The geophones (SmartSolo nodes), with a natural frequency of 5 Hz and a flat response to velocity above ~10 Hz, recorded at 1000 samples per second (see Supplementary Material Figs. S2 to S4 for a comparison of sensor responses and recorded waveforms). These nodes have an integral GNSS timing unit, and were deployed directly into the soft earth such that the top of the unit was flush with the ground surface (or just below); care was taken to ensure voids were not left around the geophones. During FSCT, 40 nodes were deployed in a ring approximately 200 m from the centre of the shotpad (Fig. 1b) and six were co-located with the broadband stations closest to the explosions (except TR03). The co-located sensors provided both a comparison with the broadband recordings and redundancy if the closest broadband sensors clipped (which they did for the large buried explosions).

The seismic network recorded signals for all eight of the FSCT explosions, with a wavefield composed of multiple body-wave paths, air-to-ground coupled arrivals, and surface waves (Figs. 4 and 5). Prior to analysis the instrument response was deconvolved from all waveform data, returning velocity seismograms in physical units; this was particularly important to allow direct comparison between geophone and broadband recordings. Arrival time picks were made manually in two two-octave passbands: [0.5,5] Hz to allow direct comparison with Ford et al. (2014, 2021) and [3,30] Hz as seismograms in this passband exhibited higher signal-to-noise ratios (while the upper frequency limit remained below the spectral corner frequency of the explosive sources). Only the initial *P*-waves exhibited impulsive arrivals (e.g., Fig. 4b and c), while later arrivals were either emergent in nature, or had low-amplitude initial arrivals that were obscured by earlier arriving energy.

4.3 Seismic Wavefield Overview

Broadband body wave arrivals were recorded for all explosions, with corner frequencies of ∼50 or 70 Hz depending upon source charge mass (see Supplementary Material Fig. S5). The body wave amplitudes are a function of charge mass, HoB and propagation distance, with the most deeply buried 100 kg explosion (S2) generating the largest ground motion (e.g., Fig. 4). *P*-wave amplitude measurements are described further in Section 4.4. Recordings on sensors within 400 m of the explosions comprise an initial *P*-wave arrival propagating at ∼1.7 km/s followed by a series of coherent reflections from deeper layers (Fig. 5c). At stations beyond ∼600 m from the source, the initial *P*-wave arrival times are consistent with refractions from deeper layers (Fig. 5a,b). Following the initial refracted arrival, a larger amplitude, temporally extended, wave packet propagates at ∼1.7 km/s and is interpreted as body wave energy travelling through, and reverberating within, the ∼150 to 200 m of soft sediments that overlie the denser chalk (e.g., Fig. 2).

Air-to-ground coupled arrivals, associated with the arrival of the atmospheric air-wave at the station, are observed propagating across the network with velocities of ∼345 m/s for both the above surface and near-surface explosions (S3 to S8), with reducing amplitudes as the depth of the explosion increases. For the deepest two explosions (S1 and S2) the air-to-ground arrival is not clearly observed due to a combination of reduced signal amplitude and increased explosion-generated seismic noise (e.g., Fig. 4 for signals at TR06). A Hyperion IFS-3000 microbarometer, co-located with the seismic sensors at TR06, allowed air-to-ground coupling coefficients to be estimated via comparison of time domain peak-to-peak amplitudes. In the 2 to 4 Hz passband the coupling coefficient is estimated to be $\sim 8\times10^{-6}$ m/(s Pa), consistent with measurements in other areas of low-velocity near-surface sediments (e.g., Wills et al., 2022).

A surface wave packet, with energy in the 1 to 4 Hz passband, arrives after the coupled airwave. For the below ground explosions, this surface wave packet comprises two prominent branches: a lower frequency (1.0 to 1.5 Hz) normally dispersed branch that starts almost co-incident with the airwave (at a velocity of ∼350 m/s) and a higher frequency (1.5 to 4 Hz) inversely dispersed branch that arrives with a velocity of ∼180 m/s. The branches merge to form an Airy phase at a time corresponding to a velocity of 120 m/s. For the above ground explosions the surface wave is dominated by an almost monochromatic phase (with a frequency of ∼1.75 Hz) that again arrives with source-to-station velocities of between 350 and 120 m/s. Read (2024) provides a detailed study of these surface wave arrivals, and a comparison with previous studies of such phases (e.g., Jardetzky and Press, 1952; Langston, 2004). An assessment of their amplitude variation (as a function of charge mass, HoB and source-to-receiver distance) will be the subject of a future study.

4.4 Seismic *P*-wave Amplitudes

First arrival *P*-wave displacement amplitudes were calculated from bandpass filtered instrument-corrected vertical component velocity seismograms, by integrating across the initial positive velocity pulse following the *P*-wave arrival time pick. The initial *P*-wave pulse was identified as being between the datapoint closest to the *P*-wave arrival time (t_P) and the next datapoint for which the velocity was less than that recorded at t_P. To reduce errors due to the discretization of the seismogram, the recordings were resampled using a Fourier (or sinc) interpolation with a sampling rate of 2000 samples per second; testing showed this resampling did not introduce artifacts into the initial *P*-phase pulse.

In this study we use vertical-component amplitudes. Ford et al. (2021) maximised the initial *P*-wave amplitude by rotating the three-component seismograms using a Principal Component Analysis (PCA) to identify the directional vector onto which to project the seismic waveforms. However, low signal-to-noise ratios in the [0.5,5] Hz passband at Foulness, particularly on the horizontal components, result in highly variable PCA-optimized amplitudes. In the [3,30] Hz passband, where root-mean-squared horizontal noise amplitudes have a median value 15 times smaller than in the [0.5,5] Hz passband, a comparison of vertical and PCA-optimized amplitudes across the network showed that in 90% of cases there was less than 7% difference between the two measurements. This indicates that the initial *P*-waves at Foulness are dominated by vertical motion, and that analysing vertical component amplitudes and comparing to the PCA-optimized amplitudes of Ford et al. (2021) is justifiable. The small horizontal signal amplitudes also make an across-network comparison of *P*-wave polarisation attributes difficult; we therefore restrict our analysis to vertical recordings.

Displacement amplitudes, d, recorded at Foulness do not decrease with a constant power-law gradient as a function of source-to-receiver distance, r (Fig. 6a and b). Measurements across all explosions, and both frequency bands, exhibit a near constant power-law decay gradient at distances <300 m from the source (i.e., $d{\propto}r^{-x_1}$) before the amplitudes increase to a maximum and then decay with a different power law exponent as source-to-receiver distance increases (i.e., $d{\propto}r^{-x_2}$ where $x_2{\neq}x_1$).

The power-law gradients, and the source-to-receiver distance and magnitude of the amplitude maximum, are frequency band dependent. In the [0.5,5] Hz band the amplitude maximum occurs at ∼1000 m from the source and is only ∼33% larger than the amplitude minimum that occurs at a distance of ∼700 m from the source (Fig. 6a). In contrast, the amplitude maximum for the [3,30] Hz measurements occurs closer to the source (between distances of 700 and 800 m) and is considerably larger; amplitudes at the maximum are between two and three times larger than those recorded between 300 and 400 m from the source (Fig. 6b). Estimates of the power-law exponents are made during construction of a *P*-wave amplitude model in Section 6.

We note that the distance at which the amplitudes reach a maximum, and the distance ranges in which particular power-law gradients are applicable, are a function of physical distance not scaled distance (compare, for example, Fig. 6b and d). This is consistent with the amplitude variations with distance being controlled by geometrical propagation effects (e.g., multi-pathing through layered structures) rather than an effect of the explosive source. This is explored further in Section 6 when considering the appropriate scaling of parameters within empirical models of *P*-wave displacement.

Hydrodynamic scaling of length variables is required to simplify the relationship between explosive HoB and displacement amplitudes (Fig. 6c), i.e., $\tilde{d}$ is a function of $\tilde{h}$ whereas d is not a function of h. For example, although shots S1 (a 10 kg shot at $\tilde{h}$=−1.0 m/kg$^{1/3}$) and S5 (a 100 kg shot at $\tilde{h}$=0.07 m/kg$^{1/3}$) produce comparable displacements (Fig. 6a), S1 exhibits scaled displacements that are a factor of ∼40 greater than those for S5 at a given scaled distance.

To inform our efforts to construct an empirical model for the FSCT seismic displacements, we first employ numerical modelling to identify seismic velocity profiles as a function of depth that can explain the major features of the recorded arrival times and amplitudes.

5 Modelling the *P*-wave Velocity Structure

The initial *P*-wave arrival time observations across the FSCT seismometer network can, to first order, be split into three distance ranges with approximately constant v_p: [150,800] m, [800,1300] m, and [1300,7000] m with the velocity increasing from ∼1.7 to 4.4 km/s as the distance increases (Fig. 5b). We use FSCT refraction and reflection arrival times to invert for a simple four-layer v_p model, by minimising the sum of squared residuals between 22 observations and predictions made using the Herrmann (2013) *refmod96* algorithm. Details are provided in Supplementary Material Section F and the model, referred to as our baseline four-layer model, is summarised in Table 3.

The observed amplitude variations as a function of source-to-receiver distance (Fig. 6) provide additional information to help constrain models of the sub-surface structure. Simulated *P*-wave displacement measurements have been made from waveforms generated by propagating a 0.064 s duration parabolic pulse through a suite of velocity models using the Herrmann (2013) wavenumber integration code. This modelling required a simple attenuation model, characterised by the *P*-wave quality factor, Q_p, to be developed for the sub-surface. The model is summarised in Table 3, and detailed in Supplementary Material Section G. However, tests showed that modelled *P*-wave arrival amplitudes at the frequencies and stand-off distances considered in this study are insensitive to the Q_p values employed. An example of the waveform simulation input is provided in Supplementary Material Section H.

Using the baseline four-layer model (Table 3) the initial *P*-wave onsets of the simulated waveforms provide a good fit to the arrival time data as expected, but the simulated *P*-wave amplitudes do not reproduce the observations in either the [0.5,5] Hz or [3,30] Hz passbands (Fig. 7a). In the [0.5,5] Hz passband the simulated *P*-wave amplitudes exhibit a reduced variation with distance compared to the observations. This is due to interference between the initial *P*-wave pulse and a later downward motion, likely an S_v arrival, reducing the amplitude (see Supplementary Material Section H for an illustration of this effect). At distances $>$1000 m the simulated amplitude reduces rapidly as a low-amplitude refracted arrival from the deepest model layer interface separates from the later arriving wavefield. In the [3,30] Hz passband the gradient of the simulated amplitude decay at short source-to-receiver distances ($<$350 m) is comparable to that observed. The seismic arrival pulse widths in this passband are shorter, such that the *P*- and *S*-waves do not interfere when using a nominal v_p/v_s ratio of 1.73. However, the observed increase in *P*-wave amplitudes at distances of between $\sim$400 and 1000 m from the source, with a maximum at $\sim$700 m, is not predicted. Reductions in amplitude are observed as refracted waves from successively deeper layers emerge as the initial arrival.

Increasing the model complexity by employing the Can (2020) *P*-wave velocity model (and again assuming v_p/v_s=1.73 throughout) produces simulated waveforms with similar arrival times and amplitude characteristics as the four layer model (Fig. 7b). At the lower frequencies, [0.5,5] Hz, the amplitude variations are almost identical to the four layer model. At these frequencies the *P*-wave wavelengths are $\gtrsim$350 m; consequently the waves are only sensitive to long wavelength model features, which are similar across both models to depths of $\sim$400 m (Fig. 7a). At the higher frequencies, [3,30] Hz, the simulated amplitude reductions (using the Can, 2020, model) as a function of distance exhibit similar gradients to the observations for distances $<$350 m and $>$900 m. There is also a small increase (less than a factor of two) in simulated displacements at distances of between 500 and 700 m from the source; however the maximum is not comparable in terms of amplitude or width to the observations. Modelled waveforms indicate that this amplitude increase is due to the positive interference of waves propagating approximately horizontally through the upper $\sim$100 m and refracted arrivals from the positive v_p gradient at depths between 100 and 300 m.

A large suite of models with varying v_p structures were tested to identify a velocity model that can reproduce the observed amplitude variations. Although models employing a smoothly increasing v_p gradient at depths between 100 and 300 m can explain the [3,30] Hz observations better than the Can (2020) and four-layer models, none of the simulations for which $v_p/v_s \simeq 1.73$ could successfully simulate the observed variations in the [0.5,5] Hz passband (see Supplementary Material Fig. S8 for an example of such a model). Improved results are possible if the v_p/v_s ratio is allowed to increase in the upper 150 m of the model (i.e., at depths where we expect to find predominantly alluvium and London Clay, Fig. 2). Previous studies provide a justification for using higher v_p/v_s ratios where such material is expected; measurements of v_p (Conway et al., 1984; Hight et al., 1997) and v_s (Hight et al., 1997; Lessi-Cheimariou et al., 2019) are consistent with v_p/v_s ratios greater than five. In addition, simulations of surface waves generated by FSCT also require very low v_s values of $<$360 m/s in the upper 150 m (Read, 2024). Fig. 7c shows results for our preferred model where the v_p/v_s values reduce from 8.0 to 2.0 over the upper 150 m.

The consequence of increased v_p/v_s ratios is to temporally separate the *P*- and *S*-wave arrivals propagating in the medium, such that *S*-wave arrivals do not interfere with the initial *P*-wave pulses in either passband. This results in the model being able to match the amplitude variations in both passbands, with a source moment of 3×10^{11} N·m. Undertaking a finite-difference simulation using the SW4 package (Petersson et al., 2023) utilizing our preferred velocity model (Fig. 7c) provided a complementary visualisation of the wavefield evolution. This confirmed that the increased displacement amplitudes between $\sim$400 and 800 m from the source arise due to the constructive interference of energy propagating almost horizontally through the upper 100 m of the model, and refracted energy returning to the surface from the v_p gradient between 100 and 300 m depth. Supporting information, including waveforms and wavefield snapshots are provided in Supplementary Material Sections H and I.

We recognize that our preferred model is simple, and is unlikely to be a unique solution. We have not, amongst other parameters, considered attenuation (Q) or anisotropy effects upon amplitudes. Additionally, the assumption of a 1D (depth-dependent) seismic property structure is an approximation; across Foulness Island alluvial deposits are known to infill channels incised into the top of the London Clay (e.g., Lake et al., 1986). However, our models demonstrate that the *P*-wave travel times and amplitudes are highly dependent upon the sub-surface v_p and v_s structure. In particular, the variation in *P*-wave arrival amplitude decay rate as a function of source-to-receiver distance provides a physically justifiable reason for modifying the seismic coupling models of Ford et al. (2021).

6 A Seismic Coupling Model for Saturated Sediments

Ford et al. (2014) proposed that first-arrival *P*-wave displacements, d (m), generated by near-surface explosions can be predicted from knowledge of the explosive charge mass, W (kg), source-to-receiver distance, r (m), and the height-of-burst (HoB) of the source, h (m), given the assumption that cube-root (hydrodynamic) scaling holds. Ford et al. (2021) developed the following model for seismic displacements,

$$\log\left(\tilde{d}_i\right) = \beta_1 + \beta_2 \log\left(\tilde{r}_{i,j}\right) + \beta_3 \text{logistic}\left(\beta_4 \tilde{h}_j + \beta_5\right) + \epsilon_{i,j} \tag{3}$$

where ϵ is the error vector (assumed to be normally distributed). Natural logarithms are used throughout, and the subscripts refer to the i^{th} station, and j^{th} explosion. The logistic function, logistic (x), is given by $1/\left(1+e^{-x}\right)$. Recall that the over tilde indicates a parameter that has been scaled by the cube root of the charge mass.

The model (eq. 3) is structured such that β_1 contains information about the shotpoint geological conditions; it is a prediction of the near-source seismic displacement generated by a fully coupled explosion. β_2 describes the decay of signal displacement as a function of distance. The $\beta_3\text{logistic}\left(\beta_4 \tilde{h}_j + \beta_5\right)$ term models the expected reduction in amplitude as the HoB value increases; β_3 describes the magnitude of the signal amplitude reduction between deeply buried and significantly above-ground explosions, while β_4 and β_5 describe the rate of amplitude decrease as a function of HoB.

β_n are five parameters $(1 \leq n \leq 5)$ to be estimated, and Ford et al. (2021) showed that the values of β_n depend upon the geological media in, or over, which the explosion has occurred (and in which the seismic waves have propagated). Guided by the data available to them, Ford et al. (2021) assumed that β_n do not change as a function of source-to-receiver distance, r. Displacement measurements indicate that this is not the case at Foulness (Fig. 6). Here we make the assumption that β_m, where $m = 1, 2$ carry information about propagation between source and receiver and will be dependent upon r, but β_p, where $p = 3, 4, 5$ will be a function of shotpoint geology only. Under these assumptions the model (eq. 3) can be updated to,

$$\log\left(\tilde{d}_i\right) = \beta_1\left(r_{i,j}\right) + \beta_2\left(r_{i,j}\right) \log\left(\tilde{r}_{i,j}\right) + \beta_3 \text{logistic}\left(\beta_4 \tilde{h}_j + \beta_5\right) + \epsilon_{i,j} \tag{4}$$

Given the FSCT displacement amplitude observations (Fig. 6), and guided by the modelling results in Section 5, we make the simplifying assumption that at Foulness $\beta_1(r)$ and $\beta_2(r)$ can be considered constant across restricted ranges of source-to-receiver distance where displacement amplitude decay can be approximated by a power-law (i.e., $\tilde{d} \propto \beta_1 \tilde{r}^{\beta_2}$). We note that this complicates the interpretation of the model. An attractive property of the Ford et al. (2021) formulation (eq. 3) is that all terms scale hydrodynamically. For the updated model (eq. 4) this is not the case; the amplitude variations are a function of r.

At Foulness we define two distance ranges in which $\beta_m(r)$, where m=1,2, can be considered approximately constant,

$$R_1 = [140, 300]\,\mathrm{m}$$

$$R_2 = [1000, 7000]\,\mathrm{m}$$

The amplitudes in the distance range between R_1 and R_2 (i.e., 300 to 1000 m) exhibit variations that are not consistent with a power-law decay, and are not considered in the simple *P*-wave displacement model constructed here. Numerical modelling results (Section 5) suggest the non power-law amplitude variations are due to the initial *P*-wave in this source-to-receiver distance range being the superposition of direct waves propagating through the upper sediments and arrivals refracted from a v_p gradient at depth.

Due to the higher density of datapoints in R_1 compared to R_2 (Fig. 6) we adopt a two-step procedure to estimate the β parameters. We first undertake a non-linear least squares inversion, employing a Levenberg-Marquardt algorithm (Newville et al., 2023), using only data from distance range R_1 to estimate β_{n,R_1}, where $n = 1, \ldots, 5$. Assuming that $\beta_{p,R_1} = \beta_{p,R_2}$, where $p = 3, 4, 5$ (i.e., the source-dependent terms), we fix β_p and then employ the same non-linear least squares inversion method using data from distance range R_2 to estimate β_{m,R_2}, where $m = 1, 2$ (i.e., the distance-dependent terms). Estimates of the β parameters, and the associated covariance matrices, are provided in Tables 4 and 5 for the [0.5,5] Hz passband allowing for direct comparison to the Ford et al. (2021) parameters (results for the [3,30] Hz passband are provided in Supplementary Material Tables S3 and S4). Prediction intervals for $\tilde{d}$ are estimated using both the Delta method (e.g., Xu and Long, 2005) and a parametric bootstrapping technique. Results from the two methods are broadly similar, so we show only 95% prediction intervals estimated using the Delta method in subsequent plots.

The best-fit model is compared to observations in Fig. 8. For distance range R_1 the logistic curve function (eq. 4) captures the variability in the observations as a function of $\tilde{h}$ (Fig. 8a), with the 95% prediction interval limits for $\tilde{d}$ being a factor of $\sim$1.7 below and above the mean model at $\tilde{h}$=0. For explosions close to the surface there is some evidence that a more rapid change occurs in $\tilde{d}$ than can be accommodated by the estimated logistic function; $\tilde{d}$ measurements for S4 ($\tilde{h} = -0.15\,\mathrm{m/kg}^{1/3}$) are higher than the predicted mean model, while $\tilde{d}$ measurements for S5 ($\tilde{h} = 0.03\,\mathrm{m/kg}^{1/3}$) are slightly lower. However, this variability is captured by the prediction interval estimates.

Given the experimental limits on achievable HoB, the data do not fully constrain the logistic curve asymptotes. Despite this, the predicted $\tilde{h}$ values at which full coupling (for negative $\tilde{h}$) and maximum decoupling (for positive $\tilde{h}$) occur are broadly similar to those found by Ford et al. (2021). These full coupling and maximum decoupling limits should only be considered valid over a restricted near-surface HoB range (which has yet to be fully determined). For deeply buried explosions the seismic amplitude will decrease due to overburden effects (e.g., Ford and Walter, 2013), and for high-altitude bursts no observable *P*-wave displacement from near-epicentre coupling is expected.

The model fit to the observations as a function of source-to-receiver distance confirms that a single power-law amplitude decay with distance is not applicable at Foulness (Fig. 8b). For measurements in the [0.5,5] Hz passband, the direct wave in the upper geological layers that generates the first arrival across R_1 exhibits a decay parameter $\beta_{2,R_1} = -3.1$, whereas the first arriving refracted arrival in R_2 exhibits a slower decay with distance given by $\beta_{2,R_2} = -2.2$. The sparser data, and larger amplitude variability, in R_2 leads to a wider $\tilde{d}$ prediction interval when compared to R_1: for $\tilde{h} = -0.3\,\mathrm{m/kg}^{1/3}$ the ratio of the upper to lower 95% prediction interval limits is 2.9 in R_1 (at $\tilde{r} = 40\,\mathrm{m/kg}^{1/3}$) whereas it equals 4.2 in R_2 (at $\tilde{r} = 300\,\mathrm{m/kg}^{1/3}$).

The model variations as a function of HoB are qualitatively similar across the FSCT and Ford et al. (2021) geological settings (Fig. 9); the most rapid reductions in $\tilde{d}$ are predicted as the HoB increases from a burial of $\tilde{h} \sim -0.5\,\mathrm{m/kg}^{1/3}$ to a height of $\tilde{h} \sim 0.3\,\mathrm{m/kg}^{1/3}$ (Figs. 9a & b). However, the change in $\tilde{d}$ between fully coupled (deeply buried) explosions and detonations at, or above, the surface is highly dependent upon geology, as found by Ford et al. (2021). Recognizing that $\tilde{d} = \tilde{d}\left(\tilde{h}, \tilde{r}, r\right)$ (eq. 4), a predicted decoupling factor, $\gamma\left(\tilde{h}\right)$, can be defined as,

$$\gamma\left(\tilde{h}\right) = \frac{\tilde{d}\left(-2, \tilde{r}, r\right)}{\tilde{d}\left(\tilde{h}, \tilde{r}, r\right)} \tag{5}$$

and represents the reduction in scaled displacement in comparison to a fully coupled, deeply buried, explosion. Decoupling factors for surface explosions, $\gamma\left(0\right)$, and example above-ground explosions, $\gamma\left(1\right)$, are given in Table 6; these suggest that saturated ground conditions, such as the wet estuarine sediments at Foulness (Section 3) and those constraining the wet-rock model of Ford et al. (2021), lead to higher variations in near-surface coupling than soft or hard dry rock. For example, the surface explosion decoupling factor, $\gamma\left(0\right)$, at Foulness is estimated to be 22, compared to the soft-rock model of Ford et al. (2021) for which $\gamma\left(0\right) = 2.3$.

The absolute value of $\tilde{d}$ at a given $\tilde{h}$ (and the relative value compared to other geologies) is highly dependent upon the distance (i.e., $\tilde{r}$) at which the measurement is made. This is particularly pronounced when comparing FSCT results with those from Ford et al. (2021) due to the difference in amplitude decay with distance in the models, as captured by parameter β_2 (e.g., Figs. 9c & d). At Foulness $\beta_2 = -2.2$ at $\tilde{r} \geq 200\,\mathrm{m/kg}^{1/3}$, whereas the three Ford et al. (2021) models have β_2 values between -1.1 and -1.3. Consequently, at short stand-off distances from an explosion (e.g., $\tilde{r} = 220\,\mathrm{m/kg}^{1/3}$) the FSCT model predicts $\tilde{d}$ at $\tilde{h}$=0 that are a factor of 4.4 greater than the Ford et al. (2021) wet-rock model (Fig. 9a), but as $\tilde{r}$ increases to 800 m/kg$^{1/3}$ the difference between the predicted $\tilde{d}$ for surface explosions reduces to ∼15% (Fig. 9b). At further distances the predicted $\tilde{d}$ for Foulness conditions will become lower than those predicted by the Ford et al. (2021) models.

Although the difference in β_2 values between this study and Ford et al. (2021) is large, numerical modelling of the initial *P*-wave phases at Foulness (Section 5 and Fig. 7) show amplitude decay rates with distance that are consistent with β_2 values ≤ -2. The difference between the FSCT and Ford et al. (2021) β_2 values is discussed in Section 7.

7 Discussion

The FSCT explosions occurred within, or above, soft saturated estuarine sediments. The measured PPV decay with distance at Foulness (Fig. 3) confirms that the propagation conditions close to the source ($\tilde{r} < 40$ m/kg$^{1/3}$) are consistent with previous ground shock studies in saturated sandy clays (Department of the Army, 1986, TM 5-855-1). Therefore, we are confident that the FSCT provide results that are complementary to recently developed models of seismic coupling as a function of HoB in hard rock, soft rock and wet (water) environments (Ford et al., 2021). A comparison of the FSCT results with the models in other geological settings can be divided into two components: the effects of near-source coupling and local seismic propagation.

7.1 Near-source coupling effects

The near-source coupling effects can be posed as two inter-related questions: (1) what is the predicted seismic displacement for a fully-coupled (i.e., deeply buried) explosion, and (2) what is the expected reduction in displacement as the HoB of the explosion increases?

7.1.1 Estimated displacements for fully coupled explosions

In eq. 4, information regarding the near-field displacements expected for a fully coupled source is captured by β_1. Comparing β_1 values for FSCT (β_{1,R_1} =0.04) and the Ford et al. (2021) models (-11.4< β_1 <-9.6) indicates very large differences between the expected displacements in the [0.5,5] Hz passband at $\tilde{r}$ =1 m/kg$^{1/3}$. However, because the seismic measurements are restricted to $\tilde{r}$ >30 m/kg$^{1/3}$, the β_1 values are highly sensitive to the estimate of parameter β_2: the rate of *P*-wave displacement reduction with distance. As noted in Section 6 the β_2 values in Ford et al. (2021) ($-1.3< \beta_2 < -1.1$) are considerably less than those identified for Foulness ($\beta_{2,R_1} = -3.07$, $\beta_{2,R_2} = -2.16$), consistent with lower β_1 values for the Ford et al. (2021) model (see, e.g., Fig. 9c and d). The data slices shown by Ford et al. (2021) illustrating displacement reduction with distance (their Fig. 13, upper right panel) do not, in our opinion, provide a good fit between model and data for the soft- and wet-rock models. In both cases the reduction in *P*-wave displacement measurements with distance appears more rapid than the model predicts. This is consistent with earlier studies using the data; the original soft-rock model of Ford et al. (2014) found $\beta_2 = -1.74$, and the re-analysis of Templeton et al. (2018) gave an alluvium model $\beta_2 = -1.87 \pm 0.18$.

The mismatch between model and data amplitude decay with distance is particularly noticeable for the wet-rock model of Ford et al. (2021); the data point at $\tilde{r}$ =100 m/kg$^{1/3}$ that has an amplitude of ~30 nm/kg$^{1/3}$ has a displacement almost two standard deviations above the median model prediction (Fig. 13 of Ford et al., 2021). We note that FSCT displacements at similar scaled distances, which are at distances just less than those influenced by velocity gradients at depth (see Section 5), have almost identical amplitudes (~30 nm/kg$^{1/3}$, Fig. 6c). The wet model of Ford et al. (2021) was constrained using data from a series of explosions at Aberdeen Proving Ground, Maryland, US (the Humming Terrapin trials, see e.g., Stone, 2017), where Precambrian metamorphic basement rocks are overlain by between 20 and 90 m of water-saturated clays, gravels and sands (Whitten et al., 1997). We might therefore expect qualitatively similar propagation conditions for Humming Terrapin and FSCT. A future joint re-analysis of these two datasets may provide insight into whether unmodelled refraction effects should be taken into account for the Ford et al. (2021) wet model, leading to revised β_1 and β_2 estimates. To summarise, it is currently difficult to compare the near-source predicted seismic amplitudes for this study and those of Ford et al. (2021) due to the large variation in amplitude decay predictions.

7.1.2 The effect of HoB on seismic coupling

The predicted reduction in displacement as a function of increasing HoB has shown to be larger for saturated sediments (FSCT) and the Ford et al. (2021) wet-rock model when compared to (dry) soft or hard rocks (e.g., Fig. 9). The reduction in coupling for a surface explosion when compared to a deeply-buried explosion is predicted to be almost ten times larger in saturated sediments when compared to the dry alluvium underpinning the Ford et al. (2021) soft rock model (Table 6). Increased coupling for deeply-buried explosions in water and clays (Fig. 9) is consistent with observations of underground nuclear tests in different geological media (Murphy, 1996), the high seismic efficiency of underwater chemical explosions (e.g., Khalturin et al., 1998), and exploration geophysics practices of setting charges below the water table and in clays to increase explosive effectiveness (e.g., Section 7.2 Sheriff and Geldart, 1995).

Although the magnitude of predicted displacement reductions as HoB increases is dependent upon the geological setting, the scaled HoB at which decoupling occurs is less variable. The $\tilde{h}$ value at which half the full decoupling in $\log$ displacement is achieved (indicated by the ratio $-\beta_5/\beta_4$, eq. 4) is always at shallow below-ground burial depths, ranging between -0.15 to -0.03 m/kg$^{1/3}$ across the four models.

Despite the model uncertainties being highly dependent upon r, $\tilde{r}$, $\tilde{h}$ and geological setting (e.g., Fig. 9), it is instructive to look at an example to illustrate the uncertainties in yield inference associated with seismic-only models. For a station at 1665 m from a 100 kg surface explosion the mean model displacement prediction, $\bar{d}$, in the 0.5 to 5 Hz passband is 73 nm, with an associated 95% prediction interval spanning [36,150] nm. The equivalent experimental measurement (station TR07, shot S5) is 54 nm. The prediction interval is approximately $[\bar{d}/2, 2\bar{d}]$; utilising the cube-root scaling assumption this displacement interval is equivalent to an interval of $[\bar{w}/8, 8\bar{w}]$ where $\bar{w}$ is the yield estimated from $\bar{d}$. This large yield uncertainty demonstrates the difficulty in using seismic-only models for near-surface explosion yield inference, and the need for complementary models using other data sources to constrain the estimate (e.g., airblast impulse, Ford et al., 2021). In addition, we have considered a case where an appropriate geological model has been chosen by the analyst. If an incorrect model was chosen, for example if the soft rock model was used to interpret data from a saturated sediment environment, the results would be subject to a significant bias (e.g., Figure 9).

7.2 Local propagation effects

When considering the effects of local propagation upon explosively generated seismic *P*-waves, FSCT provides an example where seismic velocity contrasts at depth lead to changes in the propagation path taken by the initial *P*-wave with increasing source-to-receiver distance. At short source-to-receiver distances the initial *P*-wave is a direct arrival within the near-surface sediments. As the source-to-receiver distance increases the initial *P*-wave is associated with arrivals refracted from velocity gradients at depth (e.g., Figs. 5 and 6). A consequence of this is that models of the initial *P*-wave displacement (e.g., eqs. 3 and 4) cannot be a function of the explosion site near-surface geology alone; knowledge of the deeper geology is required. Depths to refractors control the source-to-receiver distance at which particular propagation dependent parameters (β_1, β_2) will be applicable, and presumably the material properties of the deeper layers (and the impedence contrasts between the layers) will affect the absolute amplitudes of the refracted arrivals.

The FSCT results provide an example where complex amplitude variations with distance can occur; we interpret an amplitude increase with increasing distance from the source as being generated by superposition of direct waves and refracted waves. At Foulness the observations suggest positive velocity gradients at depth enhance these amplitude variations, although such interference patterns are also possible in simple layered structures (e.g., Červený, 1966). These observations have implications for the transportability of models for interpreting explosively generated P-wave displacements at local distances.

At distances >1000 m the FSCT seismometer network has a restricted azimuthal coverage of 54° (Fig. 1), such that the model (Section 6) will not capture any azimuthal P-wave amplitude variations resulting from sub-surface structure towards the south and west. However, our measurements can be satisfactorily modelled using a sequence of horizontal layers, in agreement with previous geological interpretations (see Section 3). At other locations three dimensional sub-surface structural features may lead to more complex P-wave amplitude variations that depend both on range and azimuth.

The trials described by Ford et al. (2014) and this study (FSCT) were designed with the purpose of constraining model parameters that could then be applied to rapid post-event analysis of seismic data from explosions in locations with similar near-surface rocks or soils. The FSCT results suggest that caution will be required when applying these models to geographical areas for which validated models are not available.

Due to the increasing density of seismometer networks, seismological studies of accidental or terrorist explosions occasionally have a small number of recordings at distances <10 km, (e.g., Koper et al., 1999; Zhao et al., 2016) for which relationships such as those developed in Ford et al. (2021) and this study may be applicable for explosive yield estimation. However, it is perhaps more common for seismological investigations of explosions to only have access to recordings at distances at tens of kilometres, or further, from the detonation (e.g., Pilger et al., 2021; Song et al., 2022; Nippress et al., 2023). In these cases one might calculate a seismic magnitude and utilize an appropriate magnitude-to-yield relationship (validated for fully coupled explosions) to which a decoupling factor can be applied to account for the explosion being close to the surface (see, e.g., Khalturin et al., 1998). As the decoupling factors estimated in experiments such as FSCT (e.g., Table 6) are only dependent upon the source geology and explosive height-of-burst, they may be suitable for wider application within magnitude-to-yield relationships. However, many regional magnitude scales are not based upon *P*-wave displacements, and the applicability of *P*-wave decoupling factors to other phases (e.g., L_g) has not been verified. A further complication is that where local and regional *P*-wave magnitude scales exist (e.g., Green et al., 2020) there are not always well constrained magnitude-to-yield relationships available for fully coupled explosions.

8 Future Studies

Seismic propagation within layered geologies leads to complex variations in *P*-wave amplitudes as a function of distance from the source. In such settings where there are not significant lateral variations in seismic properties (e.g., Foulness), surface wave amplitudes may exhibit a simpler decay relationship as a function of distance (e.g., Bonner et al., 2013b; Read, 2024). Such a scenario may allow a site-specific empirical relationship, of the form proposed by Ford et al. (2021), to be developed linking charge mass, source-to-receiver distance, and HOB to surface wave amplitude. Such a relationship would have the advantage that hydrodynamic scaling laws would be applicable across all distances, although the effects of along-path attenuation (Q) may have to be accounted for. Testing whether such a relationship exists for the FSCT surface wave recordings will motivate a future study.

A comprehensive analysis of FSCT high-speed video and laser scan data would also be beneficial, as it would likely provide constraints on crater formation processes. Crater dimensions may provide additional constraints for explosive charge mass estimation routines (e.g., Cooper, 1976), and an understanding of the time- and length-scales of crater formation will be of interest when considering the seismic surface wave source function for near-surface explosions.

9 Concluding Remarks

Ground motion data from the eight explosions comprising FSCT provide insight into seismoacoustic energy partitioning for near-surface explosions in, and above, saturated sediments. Measurements of peak particle velocities within 100 m of the explosions are consistent with previous ground shock measurements in saturated clays.

At Foulness, the initial *P*-wave displacement amplitudes display complex variations as a function of distance away from the source, exhibiting both distance-dependent variations in the rate of decay and a distance range in which amplitudes increase to a local maximum. Numerical modelling suggests that both effects can be explained by the layered geology beneath Foulness. Seismic multi-pathing causes the initial *P*-wave to be associated with distinct paths (direct waves, refracted arrivals) within distinct ranges of source-to-receiver distance, with each propagation path exhibiting a different amplitude decay rate as a function of distance. The observed local maximum in initial *P*-wave amplitude between 700 and 1000 m from the source is shown to be the result of constructive interference, between waves propagating through the upper sediments and waves propagating along longer, faster paths that return from velocity gradients at depth. The observation of this amplitude maximum at short stand-off distances from the explosion appears to be associated with the high v_p/v_s ratios (i.e., values $>$5) expected for saturated London Clays. Simulations suggest that, in settings where $v_p/v_s \simeq$1.73, the interference between *P*- and *S*-waves in the [0.5,5] Hz passband at short stand-off distances would cause truncation of the *P*-wave pulse, such that the amplitude maximum would not be observed.

An aim of seismoacoustic partitioning studies is to provide simplified models for predicting *P*-wave displacements given knowledge of the explosive yield, source height-of-burst, source-to-receiver distance and near-source geological setting. To account for the observed distance-dependent effects in the FSCT dataset, we have proposed a model that extends the formulation developed by Ford et al. (2021). This updated model allows for distance-dependence by defining discrete distance ranges in which the amplitude decay with distance can be approximated by a power-law decay. Model parameters associated with the source height-of-burst remain independent of the source-to-receiver distance. At Foulness deeply-buried explosions produced near-source seismic amplitudes over an order-of-magnitude larger than those expected for sources in hard rock and dry alluvium. Additionally, the reduction in P-wave displacement for a surface explosion, compared to a tamped explosion, is approximately a factor of 20 for seismic signals in the [0.5,5] Hz passband; this is almost ten times larger than models for dry alluvium (Ford et al., 2021).

Explaining the P-wave displacement variations as a function of source-to-receiver distance at Foulness required a detailed understanding of the geological structure, and associated geophysical parameters, beneath the source region. This was aided by previous geological interpretations of borehole logs (e.g., Lake et al., 1986), targeted geophysical surveys (e.g., Can, 2020) and knowledge of wave propagation in similar environments (e.g., Lessi-Cheimariou et al., 2019). Given the difference in both amplitude decay and height-of-burst variations compared to results from other trials (e.g., Ford et al., 2021), this raises questions regarding the transportability of empirically derived P-wave amplitude relationships. In limited circumstances numerical modelling results may be able to guide an analyst. For instance, if an explosion occurred within similar media to an existing model, but at a location with different thicknesses of geological units, modelling results may help to identify distance ranges where empirical models remain applicable. However, when faced with determining the correct model for a locality where little is known about the subsurface structure, care will need to be taken to address the uncertainties related to transporting the empirical relationships.

Acknowledgments

We thank Sean Ford, an anonymous reviewer, and our editor, Anne Obermann, for their insightful comments that improved earlier versions of this manuscript.

We thank representatives from the UK Ministry of Defence, QinetiQ, AWE and Spurpark Ltd. whose expertise and commitment ensured the successful firing of the Foulness Seismoacoustic Coupling Trials. Technical field support and logistics were provided by Spurpark Ltd, and Andrew Pretorius, University of Leeds. Colleagues at AWE Blacknest, in particular Sheila Peacock, are thanked for data management assistance.

We thank Professor Graham Stuart, Samuel Greenwood and James Ward for their participation in pre-trial geophysical surveys conducted by the University of Leeds.

Author contribution statement: DG & SN identified the overarching research need. DG, SN, RC, CT, AN & BS worked together to develop the trials and data collection methodology. DG, SN, AN, CT & BS were part of the team that undertook the data collection in the field during the FSCT trials, with SdR providing access to extra sensors. CT provided trials leadership and supervision. RC & SN undertook pre-trial surveys, and TCP analysed the resulting data. DG, SN, ER, NB, JW & NT contributed to signal analysis, software development and numerical modelling efforts. AN & DG coordinated the data curation activities. DG wrote the original manuscript draft; all authors contributed to reviewing & editing.

AN was funded by NERC (REMIS: Reliable Earthquake Magnitudes for Induced Seismicity, NE/R001154/1; MC^2: Mantle Circulation Constrained, NE/T012684/1), JW and NT were funded by UK Science and Technology Facilities Council grant ST/W002523/1.

Data Availability Statement

Borehole records can be found within the British Geological Survey's National Geoscience Data Centres collection: https://www.bgs.ac.uk/information-hub/borehole-records/

From mid-2025 all seismic data will be available via the EarthScope Consortium Web Services (https://service.iris.edu/), stored with the following seismic network reference: 5F, Green and Nowacki (2021), or upon reasonable request to the corresponding author (dgreen@blacknest.gov.uk).

References

Banda E, Deichmann N, Braile LW, Ansorge J (1982) Amplitude Study of the P_g Phase. J Geophys 51:153–164

Bell FG, Culshaw MG, Cripps JC (1999) A Review of Selected Engineering Geological Characteristics of English Chalk. Eng Geol 54(3-4):237–269, doi:10.1016/S0013-7952(99)00043-5

Bonner J, Waxler R, Gitterman Y, Hofstetter R (2013a) Seismo-Acoustic Energy Partitioning at Near-Source and Local Distances from the 2011 Sayarim Explosions in the Negev Desert, Israel. Bull Seism Soc Am 103(2A):741–758, doi:10.1785/0120120181

Bonner JL, Russell DR, Reinke RE (2013b) Modeling Surface Waves from Aboveground and Underground Explosions in Alluvium and Limestone. Bull Seism Soc Am 103(6):2953–2970, doi:10.1785/0120130069

Boshier RE (1982) AWRE Foulness Underwater Range. Tech. Rep. FGE/1552, Foundation and Ground Engineering Branch, Directorate of Civil Engineering Services, Department of the Environment

Boshier RE (1983) Foulness Island, Atomic Weapons Establishment 200 Metre Small Calibre

Range (C4). Tech. Rep. FGE/1827, Foundation and Ground Engineering Branch, Directorate of Civil Engineering Services, Department of the Environment

Can T (2020) Reprocessing of a 2D Seismic Line in Foulness Island, UK, to Derive a High-Resolution Subsurface Velocity Model. Unpublished MSc Exploration Geophysics Dissertation, School of Earth and Environment, University of Leeds, Leeds, UK

Červený V (1966) On Dynamic Properties of Reflected and Head Waves in the n-layered Earth's Crust. Geophys J R Astr Soc 11(1):139–147, doi:10.1111/j.1365-246X.1966.tb03496.x

Collins A (2018) Site Characterisation of Seismic Wave Speeds of Quaternary and Tertiary Overburden and Underlying Cretaceous Chalk, Foulness Island. Unpublished MSc Exploration Geophysics Dissertation, School of Earth and Environment, University of Leeds, Leeds, UK

Conway BW, McCann DM, Sarginson M, Floyd RA (1984) A Geophysical Survey of the Crouch/Roach River System in South Essex with Special Reference to Buried Channels. Q J Eng Geol London 17:269–282, doi:10.1144/GSL.QJEG.1984.017.03.10

Cooper HF (1976) Estimates of Crater Dimensions for Near-Surface Explosions of Nuclear and High-Explosive Sources. Tech. rep., R & D Associates, RDA-TR-2604-001

Crane JM, Lorenzo JM, Shen J, White CD (2018) The Competing Effects of Stress and Water Saturation on In Situ Q for Shallow (<1 m), Unconsolidated Sand, Evaluated with a Modified Spectral Ratio Method. Near Surface Geophysics 16(2):104–117, doi:10.3997/1873-0604.2017048

Department of the Army (1986) Fundamentals of Protective Design for Conventional Weapons. Technical Manual TM 5-855-1, Department of the Army, Washington, DC, USA

Denny MD, Johnson LR (1991) The Explosion Seismic Source Function: Models and Scaling

Laws Reviewed. In: Taylor SR, Patton HJ, Richards PG (eds) Explosion Source Phenomenology, American Geophysical Union, Washington DC, pp 1–24, doi:10.1029/GM065p0001

Douglas A, Marshall PD (1996) Seismic Source Size and Yield for Nuclear Explosions. In: Husebye E, Dainty A (eds) Monitoring a Comprehensive Test Ban Treaty, Kluwer Academic Press, Dordrecht, pp 225–245, doi:10.1007/978-94-011-0419-7_19

Drake JL, Little CD (1983) Ground Shock From Penetrating Conventional Weapons. In: Proceedings of The Interaction of Non-Nuclear Munitions with Structures, U.S. Air Force Academy, Colorado, pp 1–6

Ford SR, Vorobiev OY (2023) Numerical Modelling of Air-Blast Suppression as a Function of Explosive-Charge Burial Depth. Bull Seism Soc Am 113(4):1628–1634, doi:10.1785/0120220231

Ford SR, Walter WR (2013) An Explosion Model Comparison with Insights from the Source Physics Experiments. Bull Seism Soc Am 103(5):2937–2945, doi:10.1785/0120130035

Ford SR, Rodgers AJ, Xu H, Templeton DC, Harben P, Foxall W, Reinke RE (2014) Partitioning of Seismoacoustic Energy and Estimation of Yield and Height-of-Burst/Depth-of-Burial for Near-Surface Explosions. Bull Seism Soc Am 104(2):608–623, doi:10.1785/0120130130

Ford SR, Bulaevskaya V, Ramirez A, Johannesson G, Rodgers AJ (2021) Joint Bayesian Inference for Near-Surface Explosion Yield and Height-of-Burst. J Geophys Res-Solid Earth 126(2):e2020JB020968, doi:10.1029/2020JB020968

Gamar-Sadat F, Janot L, Carotti D, Gout JM, Mascomere JP, Mikkelsen G (2016) Image Quality Enhancement Using Volumetric Q-tomography and Q-PSDM - Martin Linge Case Study. In: 78th EAGE Conference and Exhibition 2016, European Association of Geoscientists & Engineers, Th STZ0 10, doi:10.3997/2214-4609.201601575

Green D, Nowacki A (2021) Foulness Seismoacoustic Coupling Trial. DOI 10.7914/SN/5F_2021, URL `https://www.fdsn.org/networks/detail/5F_2021/`

Green DN, Luckett R, Baptie B, Bowers D (2020) A UK Local Seismic Magnitude Scale, ML^P, Using *P*-wave Amplitudes. Geophys J Int 223(3):2054–2065, doi:10.1093/gji/ggaa438

Herrmann RB (2013) Computer Programs in Seismology: An Evolving Tool for Instruction and Research. Seism Res Lett 84(6):1081–1088, doi:10.1785/0220110096

Hight DW, Bennell JD, Chana B, Davis PD, Jardine RJ, Porovic E (1997) Wave Velocity and Stiffness Measurements of the Crag and Lower London Tertiaries at Sizewell. Géotechnique 47(3):451–474, doi:10.1680/geot.1997.47.3.451

Jardetzky WS, Press F (1952) Rayleigh-Wave Coupling to Atmospheric Compression Waves. Bull Seism Soc Am 42(2):135–144, doi:10.1785/BSSA0420020135

Khalturin VI, Rautian TG, Richards PG (1998) The Seismic Signal Strength of Chemical Explosions. Bull Seism Soc Am 88(6):1511–1524, doi:10.1785/BSSA0880061511

Kim K, Pasyanos ME (2023) Seismoacoustic Explosion Yield and Depth Estimation: Insights from the Large Surface Explosion Coupling Experiment. Bull Seism Soc Am 113(4):1457–1470, doi:10.1785/0120220214

Kinney GF, Graham KJ (1985) Explosive Shocks in Air, 2nd edn. Springer-Verlag, Berlin

Koper KD, Wallace TC, Hollnack D (1999) Seismic Analysis of the 7 August 1998 Truck-Bomb Blast at the American Embassy in Nairobi, Kenya. Seism Res Lett 70(5):512–521, doi:10.1785/gssrl.70.5.512

Koper KD, Wallace TC, Reinke RE, Leverette JA (2002) Empirical Scaling Laws from Truck Bomb Explosions Based on Seismic and Acoustic Data. Bull Seism Soc Am 92(2):527–542, doi:10.1785/0120000242

Krohn CE, Murray TJ (2016) Shallow Near-Surface Effects. Geophysics 81(5):T221–T231, doi:10.1190/geo2016-0028.1

Lake R, Ellison R, Hanson M, Conway B (1986) Geology of the Country Around Southend and Foulness, Memoir for 1:50000 sheets 258 and 259. Tech. rep., British Geological Survey, London: HMSO

Langston CA (2004) Seismic Ground Motions from a Bolide Shock Wave. J Geophys Res 109(B12309), doi:10.1029/2004JB003167

Lessi-Cheimariou A, Tromans I, Hadlow N, Floyd M, Pateman J (2019) A Novel Technique for Deep Seismic Cone Tests in Challenging Ground Conditions. In: Proceedings of SECED Conference 2019: Earthquake Risk and Engineering Towards a Resilient World, Greenwich, pp 1–10

Mangriotis MD, Rector III JW, Herkenhoff EF, Neu JC (2013) Scattering Versus Intrinsic Attenuation in the Vadose Zone: A VSP Experiment. Geophysics 78(2):B49–B63, doi:10.1190/geo2012-0174.1

Murphy JR (1996) Types of Seismic Events and Their Source Description. In: Husebye E, Dainty A (eds) Monitoring a Comprehensive Test Ban Treaty, Kluwer Academic Press, Dordrecht, doi:10.1007/978-94-011-0419-7_16

Newville M, Otten R, Nelson A, Stensitzki T, Ingargiola A, Allan D, Fox A, Carter F, Michal, Osborn R, Pustakhod D, Ineuhaus, Weigand S, Aristov A, Glenn, Deil C, Mgunyho M, Hansen ALR, Pasquevich G, Foks L, Zobrist N, Frost O, Stuermer, Polloreno A, Persaud A, Nielsen JH, Pompili M, Eendebak P (2023) LMFIT: Non-Linear Least-Square Minimization and Curve-Fitting for Python (1.2.2). Zenodo, doi:10.5281/zenodo.8145703

Nippress SEJ, Nippress A, Green DN (2023) Seismoacoustic Analysis of the 7 July 2011 Abadan, Turkmenistan, Explosions. Bull Seism Soc Am 113(4):1635–1651, doi:10.1785/0120220233

Nishimura S, Jardine R, Minh N (2007) Shear Strength Anisotropy of Natural London Clay.

In: Stiff Sedimentary Clays: Genesis and Engineering Behaviour: Géotechnique Symposium in Print 2007, pp 97–110, doi:10.1680/geot.2007.57.1.49

Pasyanos ME, Ford SR (2015) Determining the Source Characteristics of Explosions Near the Earth's Surface. Geophys Res Lett 42(10):3786–3792, doi:10.1002/2015GL063624

Petersson NA, Sjögreen B (2012) Stable and Efficient Modeling of Anelastic Attenuation in Seismic Wave Propagation. Communications in Computational Physics 12(1):193–225, doi:10.4208/cicp.201010.090611a

Petersson NA, Sjögreen B, Tang H, Pankajakshan R (2023) geodynamics/sw4: Sw4, version 3.0. DOI 10.5281/zenodo.8322590

Pilger C, Gaebler P, Hupe P, Kalia AC, Schneider FM, Steinberg A, Sudhaus H, Ceranna L (2021) Yield Estimation of the 2020 Beirut Explosion Using Open Access Waveform and Remote Sensing Data. Scientific Reports 11(1):14144, doi:10.1038/s41598-021-93690-y

Prasad M, Zimmer MA, Berge PA, Bonner BP (2005) Laboratory Measurements of Velocity and Attenuation in Sediments. In: Butler D (ed) Near-Surface Geophysics, Society of Exploration Geophysicists, Houston, USA, pp 491–502, doi:10.1190/1.9781560801719.ch14

Prieux V, Brossier R, Operto S, Virieux J (2013) Multiparameter Full Waveform Inversion of Multicomponent Ocean-Bottom-Cable Data from the Valhall Field. Part 1: Imaging Compressional Wave Speed, Density and Attenuation. Geophys J Int 194(3):1640–1664, doi:10.1093/gji/ggt177

Read E (2024) Seismic Coupling of Surface Waves in Clay Sediments from Subsurface and Subaerial Explosions. Masters By Research Thesis, School of Earth Sciences, University of Bristol, Bristol, UK

Shelton TW, Ehrgott Jr JQ, Moral RJ, Barbato M (2014) Experimental and Numerical Investigations of the Ground Shock Coupling Factor for Near-Surface Detonations. Shock and Vibration 2014(789202):1–11, doi:10.1155/2014/789202

938 Sheriff RE, Geldart LP (1995) Exploration Seismology, 2nd edn. Cambridge University Press

939 Sindi M (2019) Measuring Frequency-Dependent Q for London Clay. Unpublished BSc Dissertation, School of Earth and Environment, University of Leeds, Leeds, UK

941 Smart JGO, Sabine PA, Bullerwell W (1964) The Geological Survey Exploratory Borehole at Canvey Island, Essex. Bull Geol Surv, Great Britain 21:1–36

943 Song Y, Zhao LF, Xie XB, Ma X, Du G, Tian X, Yao ZX (2022) Seismological Observations on the 2019 March 21 Accidental Explosion at Xiangshui Chemical Plant in Jiangsu, China. Geophys J Int 228(1):538–550, doi:10.1093/gji/ggab356

946 Stone R (2017) Test Blasts Simulate a Nuclear Attack on a Port. Science 355(6328):897, doi:10.1126/science.aal0839

948 Sumbler MG (1996) British Regional Geology: London and the Thames Valley, 4th edn. HMSO for the British Geological Survey, London

950 Templeton DC, Rodgers AJ, Ford SR, Harben PE, Ramirez AL, Foxall W, Reinke RE (2018) Seismic Models for Near-Surface Explosion Yield Estimation in Alluvium and Sedimentary Rock. Bull Seism Soc Am 108(3A):1384–1398, doi:10.1785/0120170145

953 Whitten CB, Swartzel SM, Miller SP, Blough K (1997) Conceptual Hydrogeologic Model of Aberdeen Proving Ground - Aberdeen Area. Tech. rep., US Army Corps of Engineers, Waterways Experiment Station, Report GL-97-16

956 Williams BJ, Brug WP, Casleton EM, Syracuse EM, Blom PS, Meierbachtol CS, Stead RJ, MacLeod GA, Bauer AL, Shao XM, Anderson DN (2021) Multiphenomenology Explosion Monitoring (MultiPEM): A General Framework for Data Interpretation and Yield Estimation. Geophys J Int 226(1):14–32, doi:10.1093/gji/ggab087

960 Wills G, Nippress A, Green DN, Spence PJ (2022) Site-specific Variations in Air-to-Ground

Coupled Seismic Arrivals from the 2012 October 16 explosion at Camp Minden, Louisiana, United States. Geophys J Int 231(1):243–255, doi:10.1093/gji/ggac184

Xu J, Long JS (2005) Confidence Intervals for Predicted Outcomes in Regression Models for Categorical Outcomes. The Stata Journal 5(4):537–539, doi:10.1177/1536867X0500500405

Zhao X, Feng W, Tan Y, Li J, Pei S, An Y, Hua W, He S, Zhao Y, Liu J, Yao Z (2016) Seismological Investigations of two Massive Explosions in Tianjin, China. Seism Res Lett 87(4):826–836, doi:10.1785/0220150229

Table 1: Information regarding the eight FSCT trial explosions. W is the TNT equivalent charge mass. Height-of-burst (HoB) values are to the centre of the charge; negative values indicate a buried charge. The positional data was surveyed using 3D scanning data, combined with a tie-point from satellite imagery, and is consistent with handheld GPS measurements. †: seismic velocities calculated using these times suggest there is a timing discrepancy for these explosions, particularly S8, of up to 0.1 s.

Shot	W (kg)	HoB (m)	Firing Time (UTC)	Latitude (°N)	Longitude (°E)
S1	10	-2.15	2021-10-19 10:08:57.226	51.579266	0.861024
S2	100	-2.32	2021-10-21 11:19:13.031	51.579820	0.861526
S3	100	-1.39	2021-10-20 11:20:50.847	51.579695	0.860821
S4	100	-0.70	2021-10-08 10:42:25.936†	51.579611	0.861615
S5	100	0.15	2021-10-07 10:59:49.288	51.579483	0.860932
S6	100	1.39	2021-10-05 11:30:52.393	51.579760	0.861179
S7	10	0.105	2021-10-04 13:57:45.564	51.579615	0.861337
S8	10	0.105	2021-10-18 10:49:30.816†	51.579469	0.861217

Table 2: Instrumentation deployed during FSCT. N is the number of sensors.

Instrumentation		N	Sampling rate (samples per second)	Distance from shotpad centre (m)	Recording period (2021)
Seismic	Broadband	12	250	360 to 6950	27-Sep to 25-Oct
	Nodes	46	1000	170 to 1640	27-Sep to 25-Oct
Accelerometers		4	$1{\times}10^6$	55 to 70	During each explosion
Blast Gauges		4	$1{\times}10^6$	55 to 70	During each explosion
Infrasound		4	100	770 to 1650	28-Sep to 22-Oct
High-Speed Video		2	10000 & 2000	95	During each explosion
3D Scanning		2	-	-	After each explosion

Table 3: The best-fitting four layer *P*-wave velocity model, constrained using *P*-wave arrival picks, and the associated *P*-wave quality factor, Q_p, estimated for the expected materials in these depth ranges.

Thickness (m)	v_p (km/s)	Q_p
7	1.18	5
195	1.70	95
230	3.15	150
Halfspace	4.40	200

Table 4: Least-squares estimates of the *P*-wave displacement model parameters (β_n, where $n = 1, \ldots, 5$, eq. 4) and the associated covariance matrix, for observations in the [0.5,5] Hz passband and the [150,300] m source-to-receiver distance range (R_1).

Parameter		β_1	β_2	β_3	β_4	β_5
Mean Value		0.04	-3.07	-4.99	3.17	0.48
Covariance	β_1	0.25	-0.045	-0.16	-0.14	-0.022
	β_2	-0.045	0.0084	0.025	0.020	0.0026
	β_3	-0.16	0.025	0.19	0.16	0.047
	β_4	-0.14	0.020	0.16	0.14	0.040
	β_5	-0.022	0.0026	0.047	0.040	0.017

Table 5: Least-squares estimates of the *P*-wave displacement model parameters (β_m, where $m = 1, 2$, eq. 4) and the associated covariance matrix, for observations in the [0.5,5] Hz passband and the [1000,7000] m source-to-receiver distance range (R_2). β_p, where $p = 3, 4, 5$, are assumed to take the same values as the inversion undertaken at closer source-to-receiver distances (Table 4).

Parameter		β_1	β_2
Mean Value		-2.17	-2.16
Covariance	β_1	1.1	-0.19
	β_2	-0.19	0.032

Table 6: Predicted decoupling factors $\gamma\left(\tilde{h}\right)$ (eq. 5) for surface, $\left(\tilde{h} = 0\right)$, and above-ground, $\left(\tilde{h} = 1\right)$, explosions.

Model		$\gamma(0)$	$\gamma(1)$
Ford et al. (2021)	Soft	2.3	3.8
	Hard	7.6	42
	Wet	13	85
FSCT (this study)		22	130

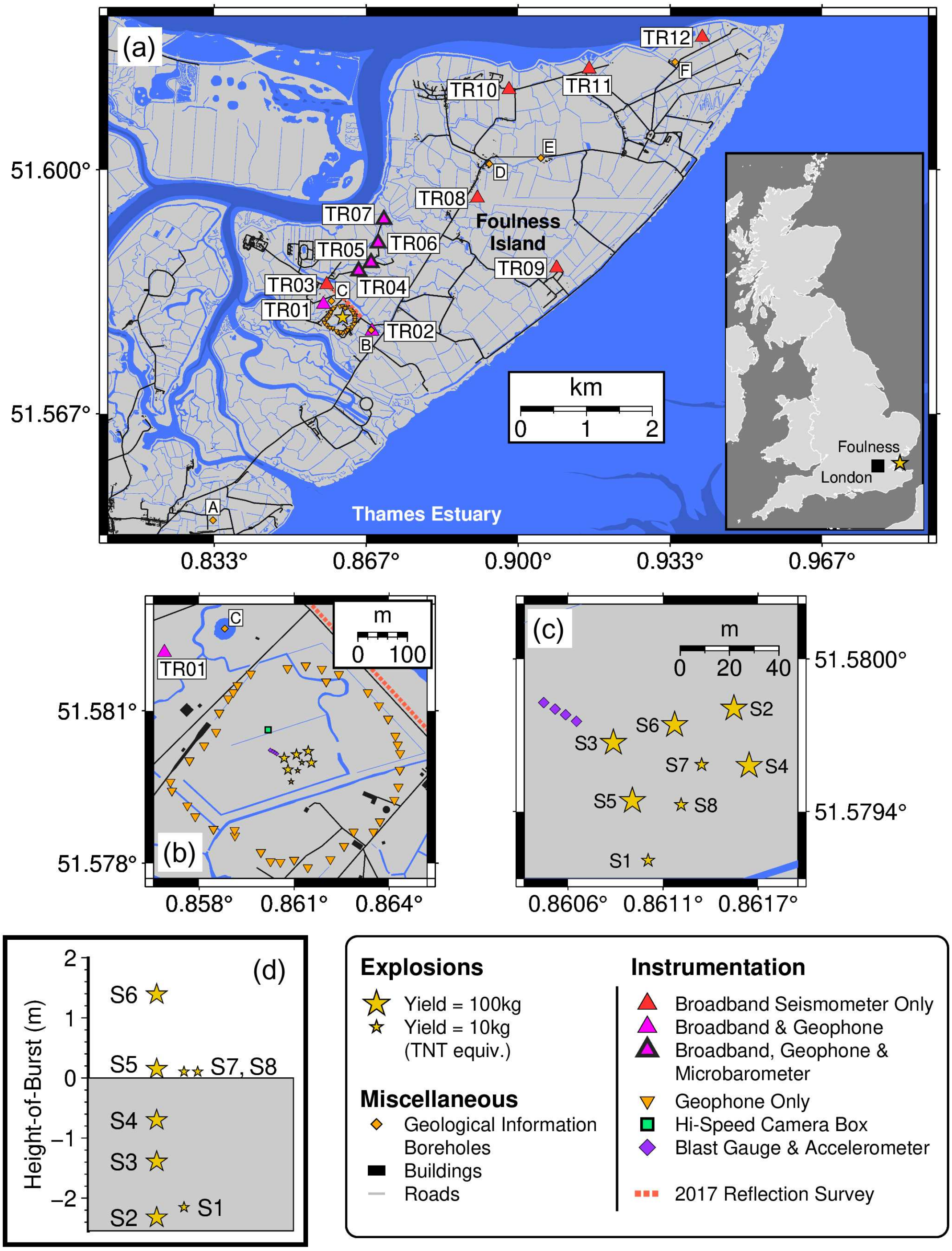

Figure 1: The layout of the Foulness Seismoacoustic Coupling Trials (FSCT) across Foulness Island (panel a), ∼70 km east of London (panel a inset). The eight explosions (S1 to S8) were contained within a 75 m by 75 m shotpad, that was surrounded by a ring of geophones (panels b and c). The explosions were detonated at heights-of-burst (HoB) of between 1.4 m above and 2.3 m below the ground surface (panel d, and Table 1). Borehole labels (A to F) correspond to those in Fig. 2. Broadband seismometer locations are labelled TR01 to TR12.

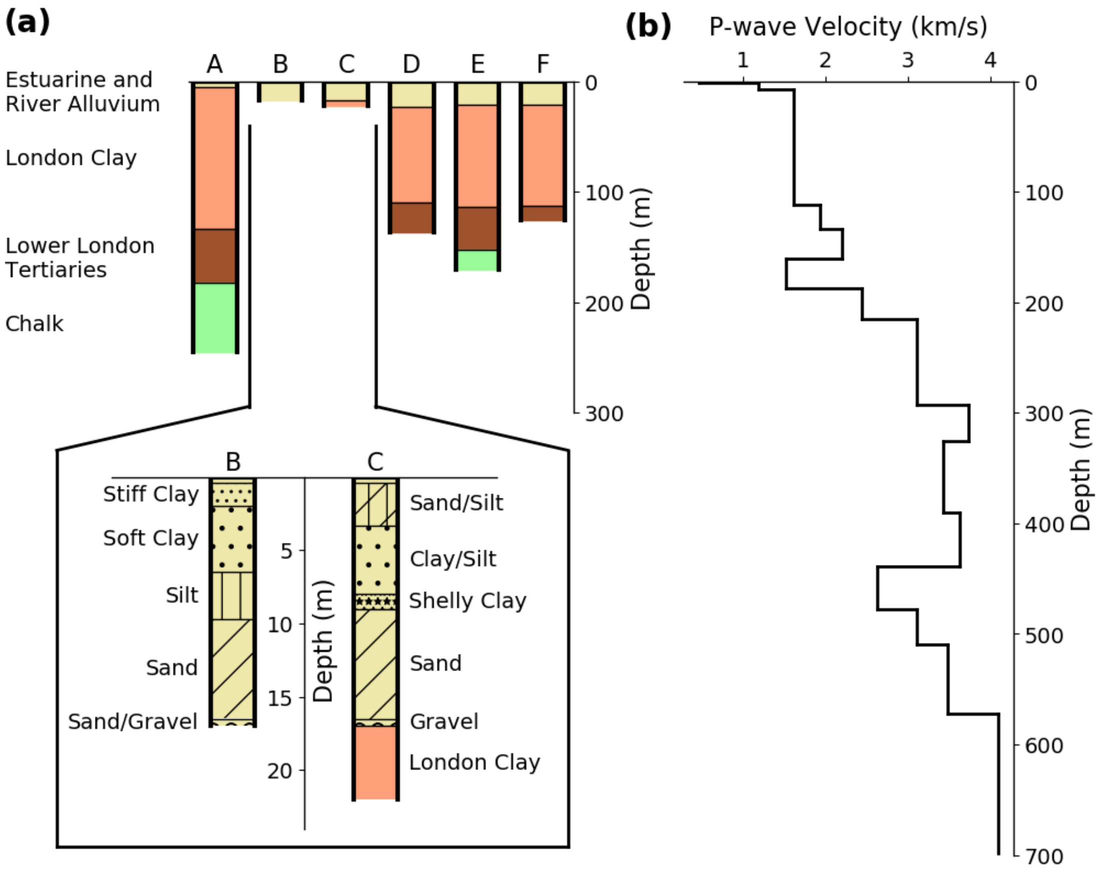

Figure 2: The geological structure beneath Foulness Island (panel a) compared to a *P*-wave seismic velocity profile (panel b) constructed from a seismic reflection survey conducted ∼300 m to the north-east of the FSCT shotpad (Can, 2020). Boreholes labels (A to F) correspond to those shown in Fig. 1a; boreholes B and C are within 500 m of the FSCT shotpad, and details of the upper 20 m sediment sequence are given at the base of panel a. Borehole summaries are based upon records provided by British Geological Survey (UKRI).

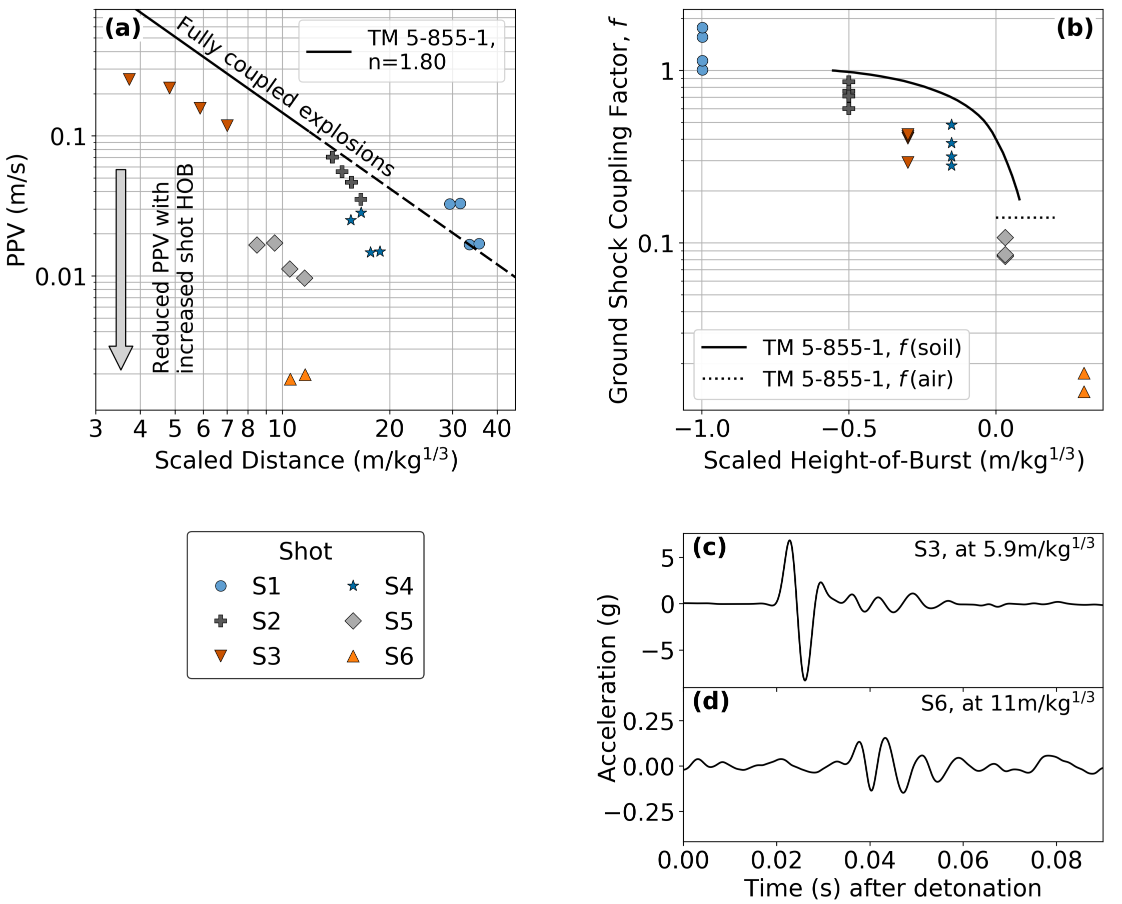

Figure 3: Vertical ground motion measured on accelerometers within 87 m of the FSCT explosions (Fig. 1c). The measured peak particle velocities (PPV) are dependent upon both the scaled distance from the source (panel a) and the height-of-burst (panel b). Only two recordings are available for shot S6. A Department of the Army (1986) model (TM 5-855-1) for ground shock generated PPV for buried explosions has been fit to the S1 and S2 data (panel a, black line: solid in distance range of original TM 5-855-1 study, dashed when extrapolated to further distances). The ground shock coupling factors are illustrated in panel b; the lines indicate the TM 5-855-1 models ($f(\tilde{h})$, eq. 1) while the data points are the ratio of the measured FSCT PPV to that predicted by the TM 5-855-1 model for a fully coupled explosion (f_{FSCT}, eq. 2). Example acceleration recordings are provided in panels c and d; positive values indicate upwards motion.

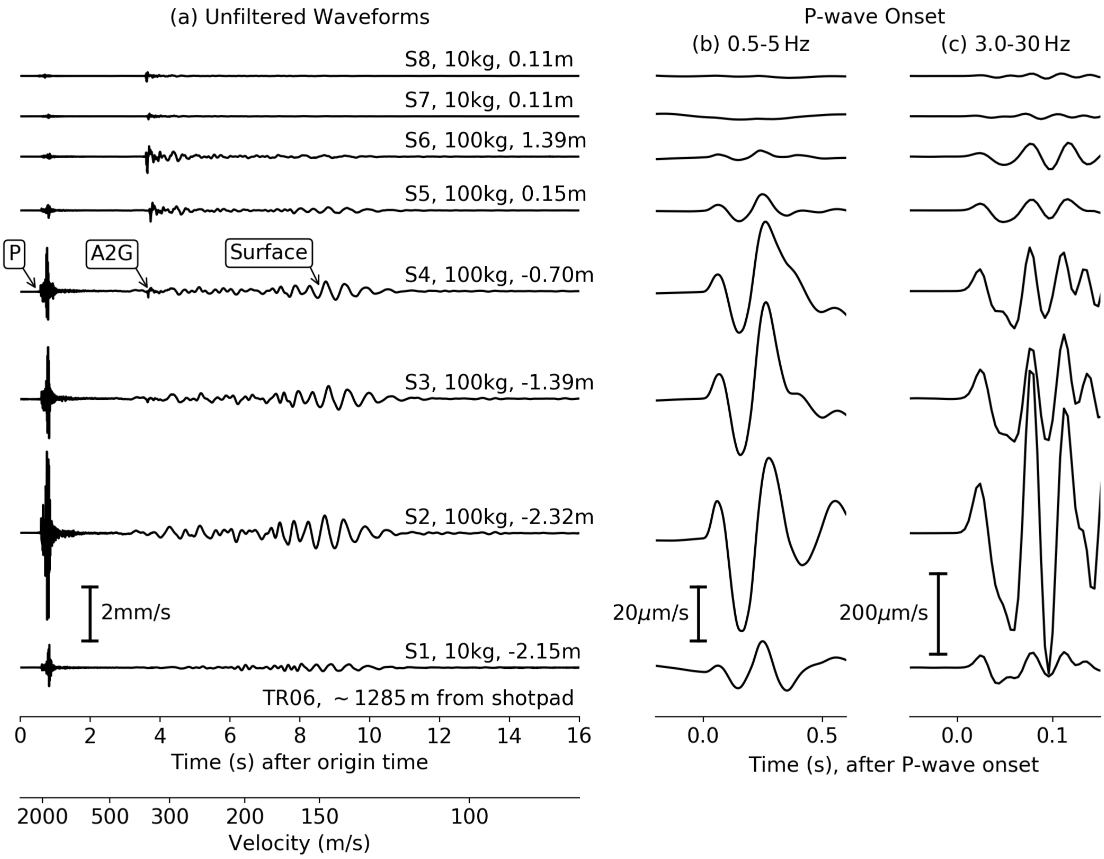

Figure 4: Velocity seismograms recorded at TR06, 1285 m from the centre of the shotpad for the eight explosions (S1 to S8). Labels to the right of panel a, showing unfiltered waveforms, indicate the explosive charge mass (kg) and HoB (m). Boxed annotations indicate the P-wave, air-to-ground coupled (A2G) and surface wave arrivals. Details of the *P*-wave onsets are shown in two passbands: 0.5 to 5 Hz (panel b) and 3.0 to 30 Hz (panel c).

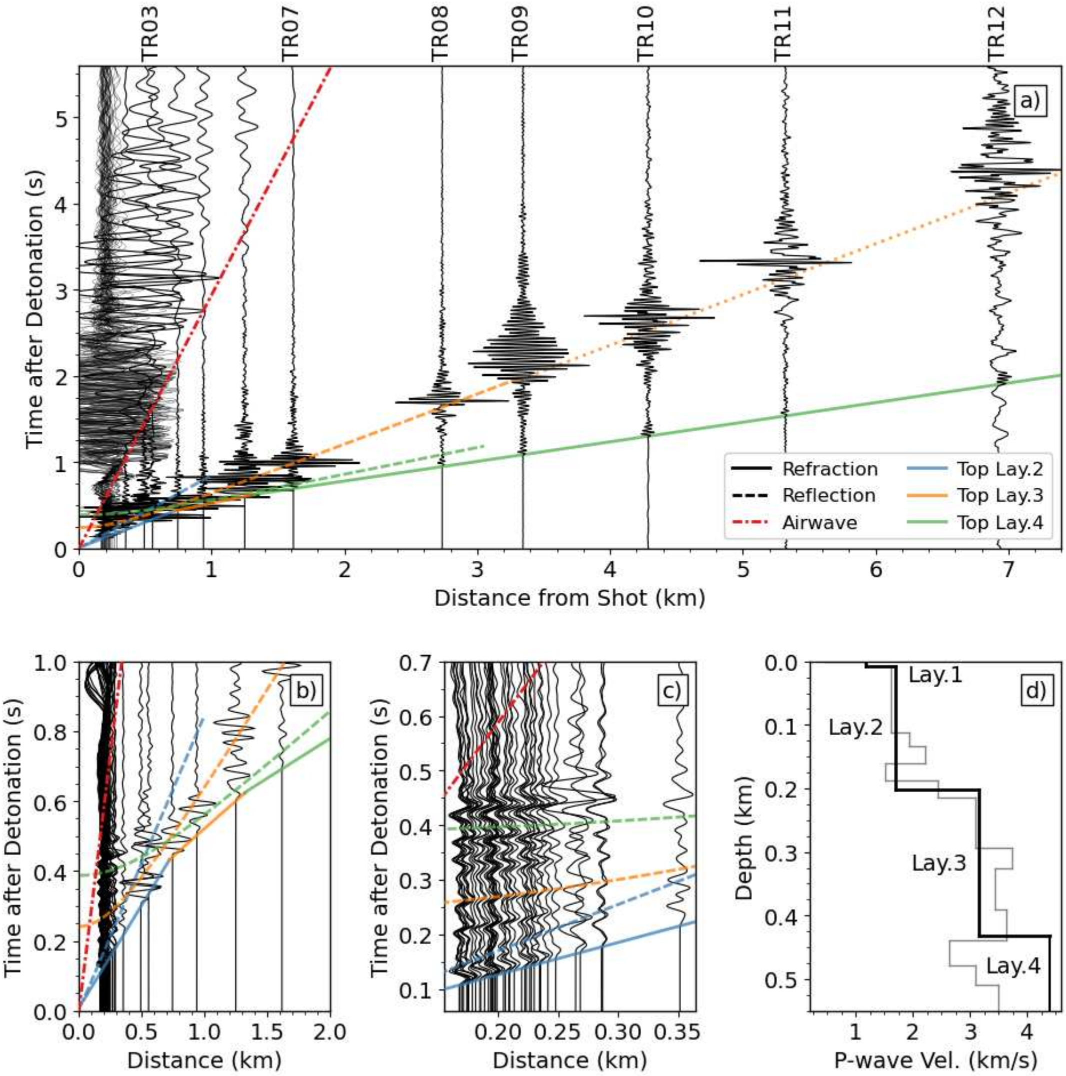

Figure 5: Seismogram record sections, bandpass filtered between 3 and 30Hz, recorded after explosion S2. The body wave packets that arrive before the airwave are shown in panel a), with arrivals from ray-tracing through the best-fitting four layer model (black line, panel d) shown as coloured lines. The dotted line that continues the reflected arrival from the top of Layer 3 out to distances greater than ∼3.5 km represents an arrival with a velocity of 1.7 km/s, i.e., a direct wave though Layer 2. Details of the near-source arrivals, out to distances of 2 km and 350 m, are shown in Panels b) and c) respectively. The thin grey line in Panel d) is the model of Can (2020).

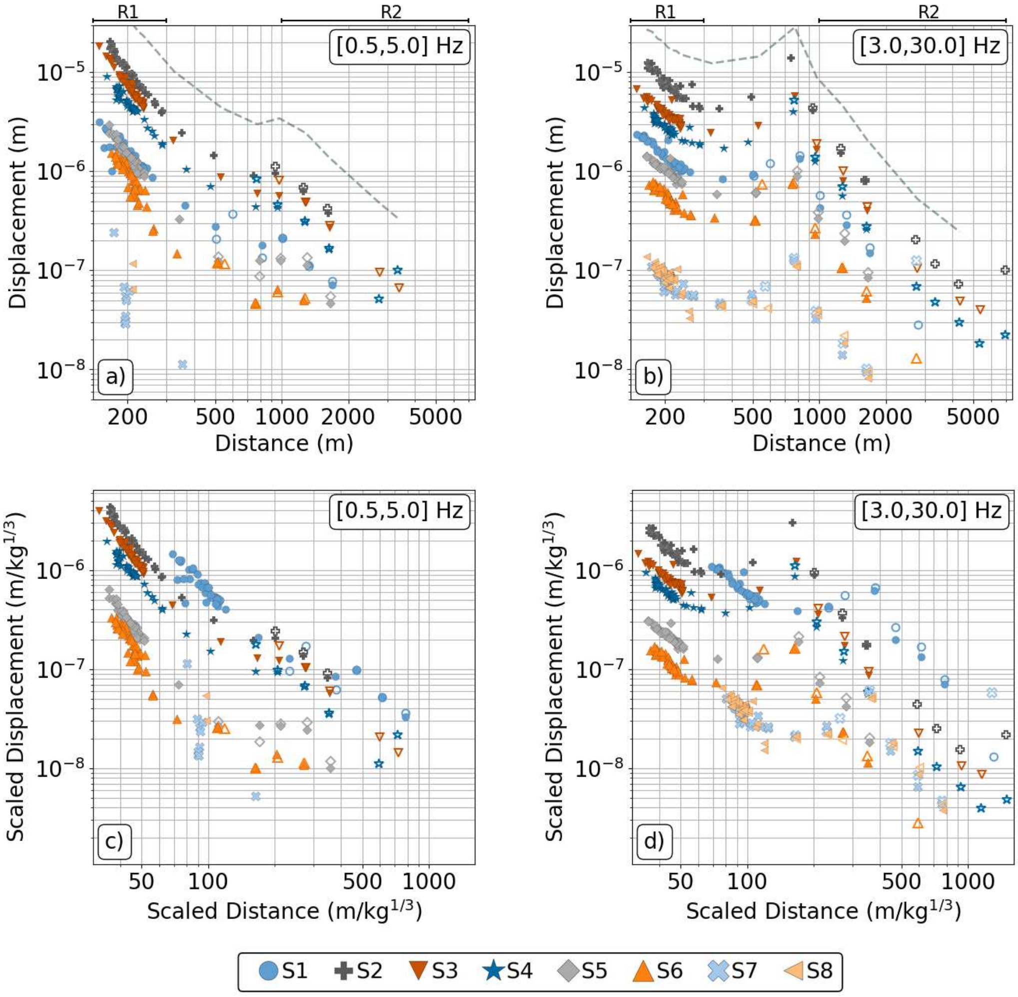

Figure 6: First arrival *P*-wave displacements across the FSCT seismic network, measured in two passbands: [0.5,5] Hz (panels a and c) and [3,30] Hz (panels b and d). Filled symbols indicate geophone nodes, open symbols indicate broadband sensors. R_1 and R_2, shown above panels a) and b), refer to the distance ranges in which models of approximately power-law distance decay are fit (Section 6). The grey dashed lines, representing a smoothed fit through the S3 data, are vertically offset from the observed amplitudes and have been added to provide a visual guide to the general form of displacement decay with distance. In panels c) and d) the underlying amplitude data are the same as that for panels a) and b), respectively; the difference is that the amplitudes and distances in the lower panels have been scaled by the cube-root of the explosive charge mass. A comma separated variable file containing the displacement measurements is provided in the Supplementary Material.

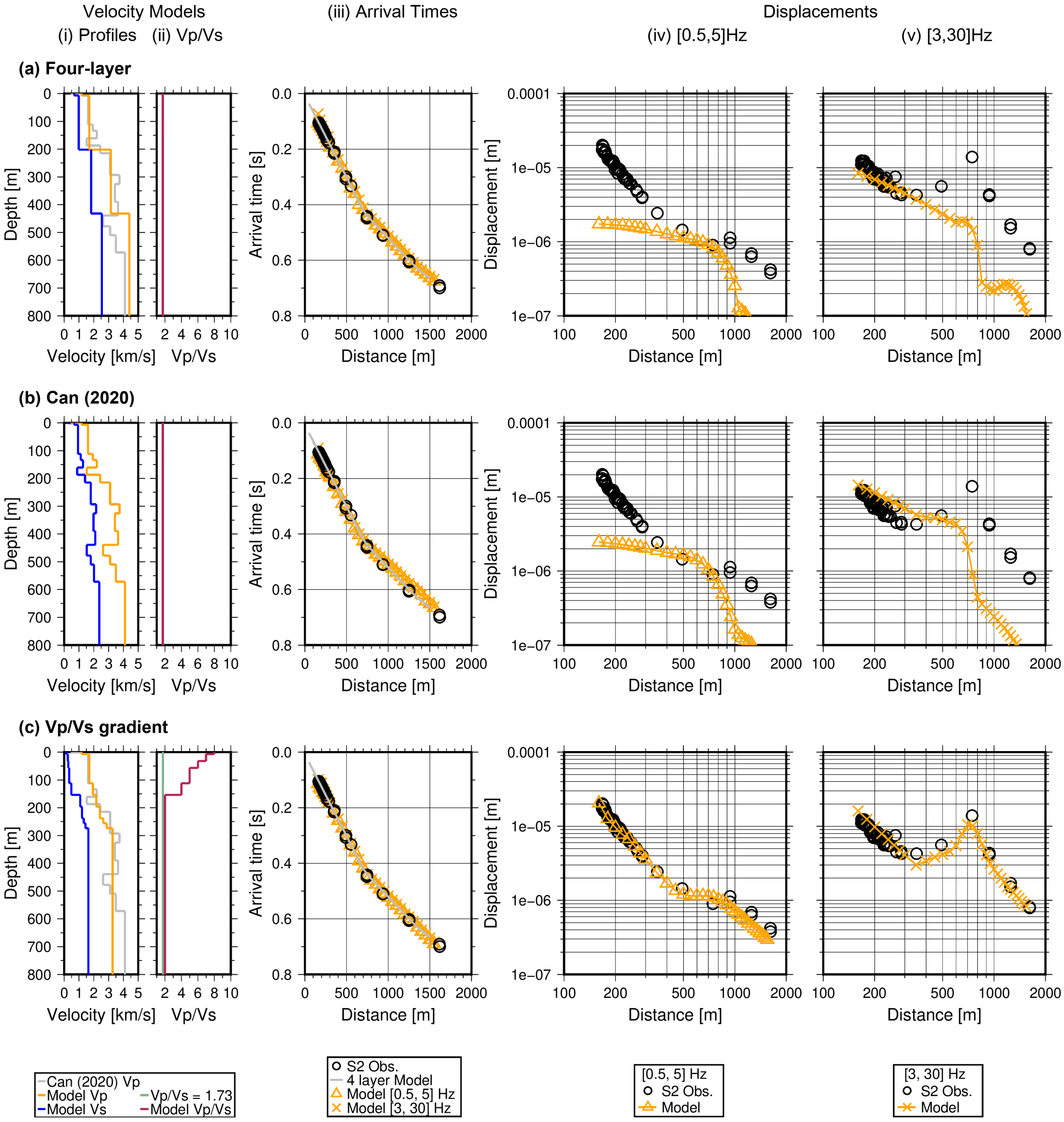

Figure 7: A comparison of arrival time and displacement amplitude observations with numerical modelling results using three simplified seismic velocity models: (a) our baseline four-layer model constrained using arrival time data only (Table 3), (b) the *P*-wave velocity model of Can (2020), with an assumed v_p/v_s ratio of 1.73, and (c) our preferred model where the v_p/v_s ratio is allowed to increase within the upper 200 m. From left to right the five panels for each model give (i) the model v_p and v_s profiles (in orange and blue respectively) in comparison to the v_p profile estimated by Can (2020) (in grey), (ii) the model v_p/v_s ratio (in maroon) in comparison to a v_p/v_s ratio of 1.73 (in green), (iii) a comparison of the observed and modelled *P*-wave arrival times, and comparisons of the initial *P*-wave amplitudes in comparison to observations for explosion S2 in the (iv) [0.5,5] Hz and (v) [3,30] Hz passbands.

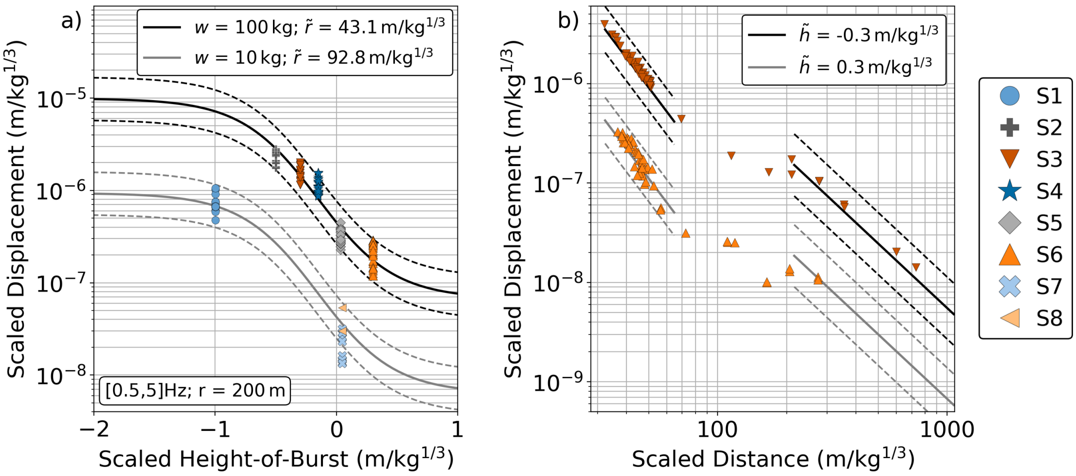

Figure 8: The scaled seismic displacement model (eq. 4) fit to the measured FSCT amplitudes in the [0.5,5] Hz passband, as a function of scaled HoB (panel a) and scaled distance (panel b). Variations with HoB (panel a) are shown at r=200 m, within a distance range for which there is a high density of geophone recordings (Figs. 1b, 6). The superimposed measured amplitudes (coloured symbols) are taken from the [180,220] m distance range. Two models are shown, corresponding to the scaled distances of the 100 kg explosions (black lines) and the 10 kg explosions (grey lines). The solid lines are the mean model, with the dashed lines representing the 95% prediction interval. Variations with scaled distance (panel b) are shown for a below ground explosion (S3, $\tilde{h}$=$-$0.3 m/kg$^{1/3}$) and an above ground explosion (S6, $\tilde{h}$=0.3 m/kg$^{1/3}$); the models are only shown across the scaled distances for which they were calculated.

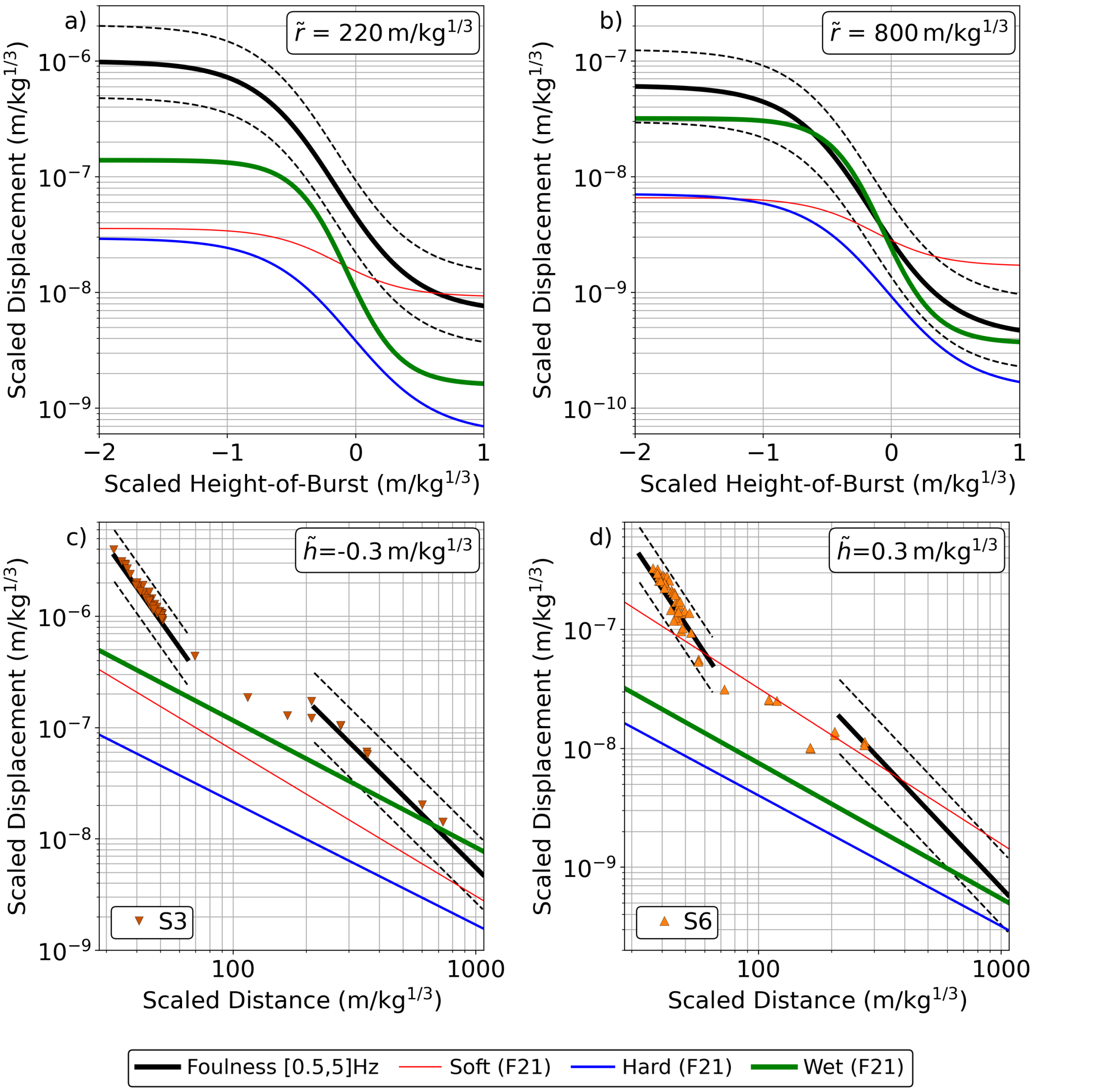

Figure 9: Comparison of the FSCT seismic displacement model (black lines) with those reported for different geological settings by Ford et al. (2021), indicated as F21 in the legend. All models are for [0.5,5] Hz passband predictions. The model variations as a function of scaled HoB are shown at scaled distances of 220 m/kg$^{1/3}$ (panel a) for comparison with Ford et al. (2021) and at 800 m/kg$^{1/3}$ (panel b) to illustrate the difference in scaled displacements at different distances from an explosion. Modelled scaled displacements as a function of scaled distance for an above-ground explosion (panel c) and a below-ground explosion (panel d) show the difference in scaled displacement amplitude for explosions at different scaled HoB. Solid lines indicate the mean model; dashed lines for the FSCT models indicate the 95% prediction interval. In panels c) and d) an explosive charge mass of 100 kg was assumed when calculating the scaled distance ranges at which the FSCT models were applicable, such that the S3 and S6 data (symbols) could be added for direct comparison.

Supplementary Material for "Seismic Waves Generated by Explosions In, and Above, Saturated Sediments: The Foulness Seismoacoustic Coupling Trials"

David N. Green[1], Stuart E. J. Nippress[1], Andy Nowacki[2], Roger A. Clark[2], Evie Read[3], Tuğçe Can Postacı[2,†], Chris Tilbury[4], Nick Benson[3], Sjoerd A. L. de Ridder[2], James Wookey[3], Nicholas A. Teanby[3], Barry Stone[4]

1. AWE Blacknest, Brimpton, Reading, UK

2. School of Earth and Environment, University of Leeds, Woodhouse Lane, Leeds, UK

3. Department of Earth Sciences, University of Bristol, Wills Memorial Building, Queens Road, Bristol, UK

4. Spurpark Ltd., Shoeburyness, Essex

†Now at General Directorate of Mineral Research and Exploration, Department of Geophysical Studies, Ankara, Turkey

Contact: David Green, dgreen@blacknest.gov.uk

A Explosive Emplacement Details

The five larger FSCT shots used 70.4 kg of HMX explosive, with four PE4 boosters each having a weight of 0.25 kg. The HMX was used in wetted form; the wetted explosive for each shot had a weight of $\sim$89 kg. The explosives were housed within a plastic liner contained within a cylindrical fibre drum. The fibre drums had a diameter of 470 mm and a height of 625 mm. For the below ground shots the height of the drum was trimmed to 550 mm. The HMX explosive filled the cylindrical drum to a height of 300 mm. For the below ground shots the remaining space within the drum was filled by two styrofoam spacers; these allowed the cabling to be inserted through the top of the drum while protecting the boosters and cabling from being crushed by the sand fill that was used to stem the boreholes.

The three small shots used 7.7 kg of PE8 explosive contained within an expanded foam casing with a diameter of 210 mm and a height of 215 mm. The base of the expanded foam casing had a thickness of 10 mm.

The below-ground emplacements were undertaken within boreholes, dug using a mechanical auger. Each borehole was lined using a single length of ridged high-density polyethylene (HDPE) pipe, to ensure that the holes dug into the soft alluvial sediments (clays, silts) did not collapse before the shot emplacement. For the 100 kg charge weight shots (S2, S3, S4) the pipe had internal and external diameters of 588 mm and 700 mm respectively. For the 10 kg charge weight shot (S1) the pipe had internal and external diameters of 302 and 354 mm respectively. Any small (<100 mm) gap between the plastic liner and the edge of the drilled hole was backfilled with sand.

Prior to the deployment of the charge any water that had collected in the base of the borehole was pumped out; the rate of water ingress was slow enough that after pumping the charge could be deployed onto a solid base. Once dry, the depth to the bottom of the borehole was measured, and a small amount of sand was placed at the borehole base to create a level surface that would ensure the depth to the centre of the charge was correct. The charges within their casings were lowered into the boreholes from a tripod, using a specially designed fabric webbing net to ensure safe and secure deployment. The cabling (firing and a fibre diagnostic) exited the top of the fibre drum and was protected by plastic conduit. Once securely deployed in the centre of the borehole, sharp sand was used to stem the borehole to surface level (taking care to ensure that no voids were left around the sides of the charge casings).

The above ground emplacements were either placed on the ground surface with a cardboard sheet laid beneath the casing to provide a stable surface (S5, S7, S8), or on a specially constructed wooden plinth designed such that the mid-point of the explosive was at the correct height (S6).

B Blast Wave Recordings

Four PCB Electronics ICP Model 113B28 pressure sensors, recording at 1×10^6 samples per second, were deployed along a radial line approximately North-West from the centre of the explosives pad (Fig. 1c, main paper). The sensor locations were not changed between explosions, such that the distances between detonation and sensor varied between 17 m (for the closest sensor to S3) and 87 m (for the furthest sensor from S4). The sensors were clamped to vertical steel poles at 5 m intervals along the radial line, with the closest to the pad positioned 1.5 m above the ground and the remaining three at 0.6 m above the ground.

Each sensor was mounted at the centre of a steel baffle, providing a smooth rigid surface (flush to the measurement diaphragm) to minimise pressure perturbations caused by edge effects. These sensor heads were rotated between explosions so that for each detonation the baffle remained parallel to a radial line originating at the explosion location.

Recordings of the surface and above ground shots (e.g., Fig. S1d) exhibit exponentially decaying waveforms. The recordings unfortunately suffered from a limited low-frequency response, leading to an underestimation of the blast impulse (as measured by the area under the positive phase of the blast signal); this appears similar to the issue noted by Ford et al. (2014) for earlier trial measurements. Ford et al. (2014) noted that, despite the difficulties in measuring blast impulse, peak pressures were less sensitive to issues with blast gauge low-frequency responses. Therefore, we provide an analysis of blast peak pressures measurements (Fig. S1).

For surface and above-ground explosion recordings, estimation of peak pressures is often hampered by the finite response time of the pressure gauge. Ford et al. (2014) addressed this by estimating the peak pressure at the blast arrival time, by extrapolating a curve fit to the exponentially decaying portion of the blast waveform. The curve fit function has the form $p\,(t) = p_0\,(1 - t_r)\exp\,(-bt_r)$ where $p\,(t)$ is the overpressure at time t (t=0 is the arrival time of the blast wave) and p_0 is the peak overpressure. $t_r = t/t_{\mathrm{dur}}$ where t_{dur} is the positive phase duration. We apply this methodology to estimate peak pressures for shots S5, S6, S7 and S8. Due to the longer rise times and lower-frequency waveforms associated with the buried explosions (e.g., Fig. S1c) we did not apply the method to recordings from shots S1, S2, S3 and S4.

Peak pressures are scaled to account for differences in ambient pressure at the explosion site during the FSCT campaign. Following Ford et al. (2014) the scaled overpressure, $\tilde{p_0}$, is calculated as $\tilde{p_0} = p_0\,(P/P_0)^{-1}$ where P is the ambient pressure at the time of the shot and P_0 is the standard atmospheric pressure of 101325 Pa. Ambient pressures, P, at the times of the FSCT shots are given in Table S1.

The results show that the surface and above ground shots are consistent with the expected overpressures from the Kinney and Graham (1985) blast model (Fig. S1a). The peak overpressures reduce rapidly with burial of the explosive. For FSCT, at HoB=$-0.4\,\mathrm{m/kg}^{1/3}$ we observe a reduction in $\tilde{p}$ of about a factor of 15, compared to a surface explosion (Fig. S1b). This is similar to the factor of $\sim$20 presented in Fig. 4 of Ford and Vorobiev (2023).

We note the difference in pressure waveform shapes for explosions at depth (e.g., Fig. S1c) compared to the blast waveforms observed for explosions at, or above, the ground surface (e.g., Fig. S1d). As explosive depth increases the waveforms become more complex, with slower signal onsets and potentially multiple positive phase maxima. The change in waveform morphology as a function of depth-of-burial has been interpreted by Ford and Vorobiev (2023) as reflecting a transition from atmospheric shock wave generated waveforms for near-surface explosions, to spall (ground-motion) generated pressure perturbations for more deeply buried explosions.

Table S1: Ground-level air temperature and pressure values for the time of each FCST shot. To convert mbar to Pa, multiply the value by 100. Data are from NASA MERRA v2 model (https://gmao.gsfc.nasa.gov/reanalysis/MERRA-2/).

Shot	Temp. (°C)	Ground Level Pressure (mbar)
S1	18.5	1013
S2	9.5	1009
S3	17.2	1000
S4	15.6	1030
S5	14.4	1027
S6	13.4	999
S7	15.4	1010
S8	15.2	1017

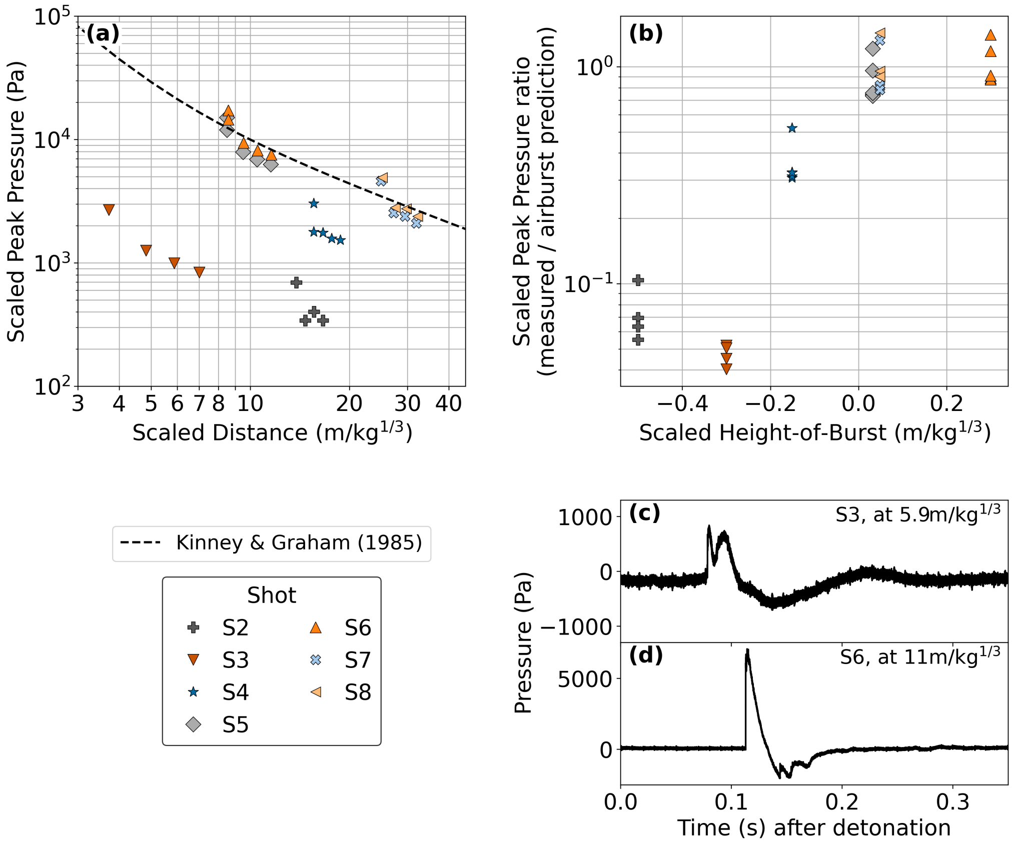

Figure S1: Peak overpressure estimates, scaled for ambient pressure conditions at the time of the shots, recorded on blast gauges within 87 m of the FSCT explosions (Fig. 1c, main paper). The peak pressures are dependent upon both the scaled distance from the source (panel a) and the height-of-burst (panel b). The Kinney and Graham (1985) model for peak overpressure generated by atmospheric chemical explosions is shown as the dashed line in panel a. The peak pressure reduction, compared to an airburst, is illustrated in panel b; the data points are the ratio of the scaled peak pressure measurements to those predicted by the Kinney and Graham (1985) model (panel a). Example pressure recordings are provided in panels c and d.

C Sensor Responses

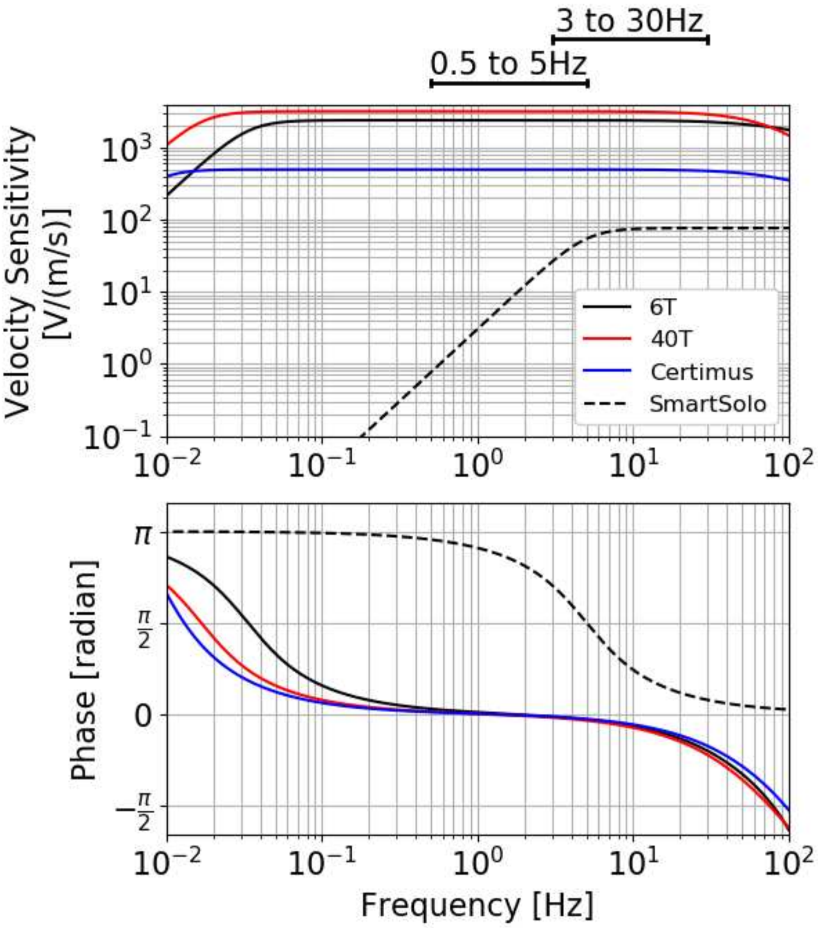

Figure S2: Instrument responses for the four types of seismic sensor deployed as part of FSCT. The geophone nodes are manufactured by SmartSolo Inc., the three broadband sensors are manufactured by Güralp Systems Ltd. The two filter passbands used in the study are provided above the plot for reference.

D Sensor Comparisons

A comparison of a co-located broadband and node pair (location: TR07, shot: S3) in the two analysis passbands for this study.

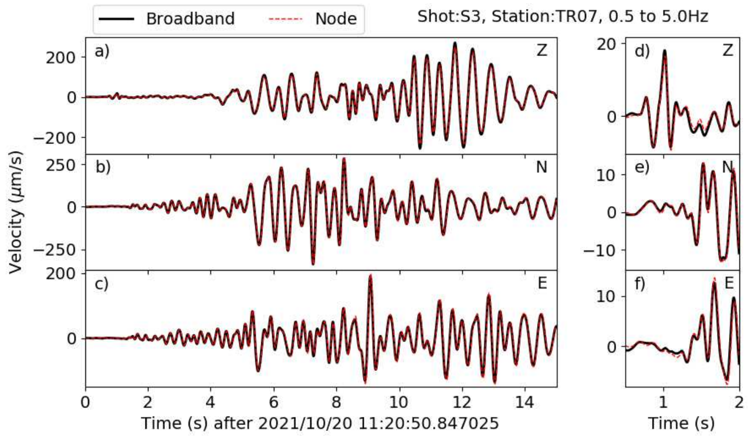

Figure S3: A comparison of three-component recordings for shot S3 on co-located broadband (Güralp Certimus) and geophone (SmartSolo) sensors. Panels a) to c) show a 15 s window for the vertical (Z), north (N) and east (E) components respectively. Panels d) to f) show the detail of the *P*-wave arrival. Traces bandpass filtered between 0.5 and 5 Hz.

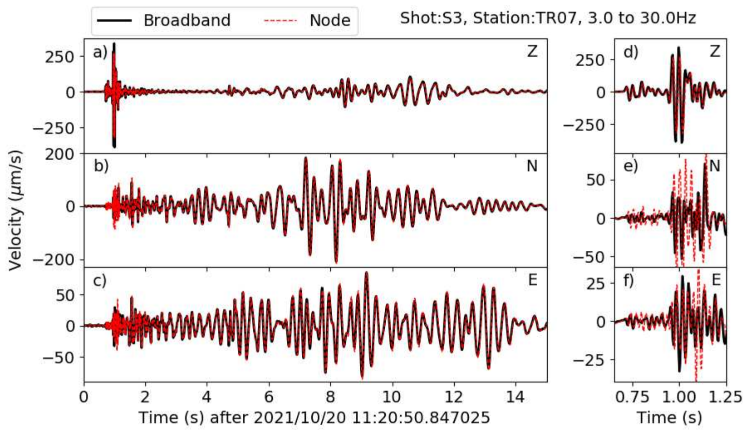

Figure S4: The same co-located broadband and geophone comparison as Fig. S3 except bandpass filtered between 3 and 30 Hz.

E Signal Displacement Spectra: TR06

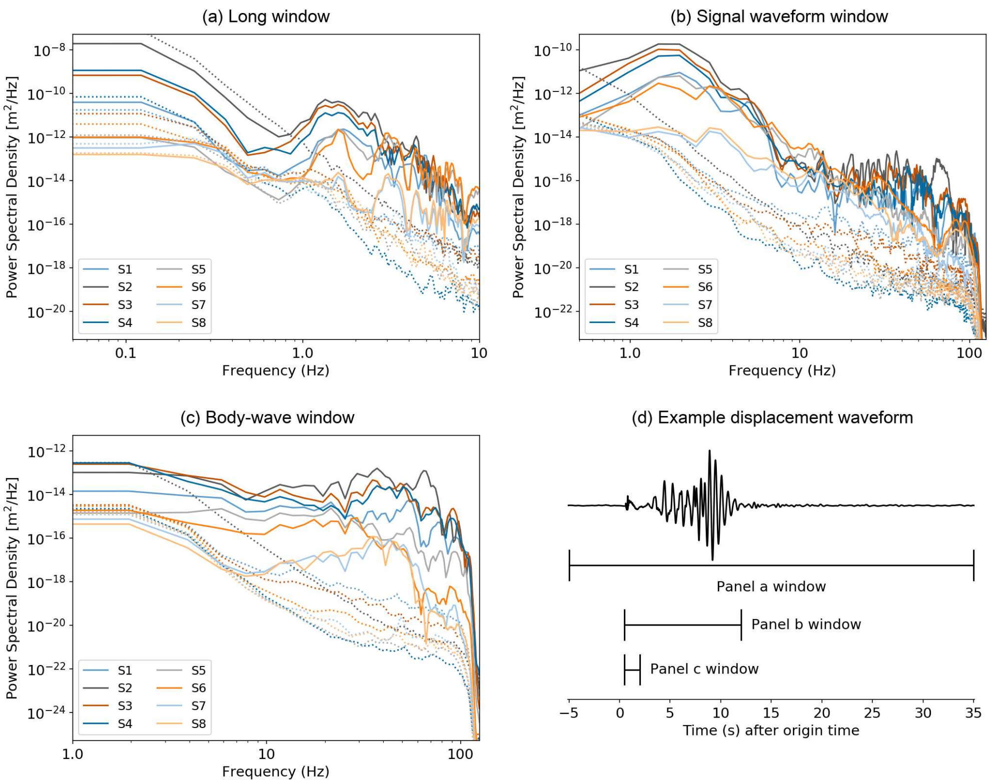

Figure S5: Spectra of the TR06 vertical displacement waveforms for all eight FSCT shots; bold lines are signal spectra, dotted lines are pre-event noise estimates. The three spectral estimates (panels a to c) focus on different portions of the waveform (panel d). Note that the spectra plots have different frequency limits. All spectra were calculated using a Welch periodogram method with windows lengths of (a) 8.2 s, (b) 2.0 s, and (c) 0.5 s; each spectral estimate employed a 75% overlap between windows.

F A simple four-layer *P*-wave velocity model for Foulness

We use FSCT refraction and reflection arrival times to invert for a simple four-layer v_p model, to be used as a baseline model when developing more complex models that can match the observed amplitude variations with source-to-receiver distance.

We assume, following Can (2020), that there is a 7 m thick layer of slow sediment (v_p =1.18 km/s) at the surface that we cannot resolve with the FSCT data. We then invert for a three layer structure beneath this. We utilize 12 first arrival time picks and 10 later arriving reflection picks at source-to-receiver distances of between 350 and 3400 m. We calculate travel times, C, using the Herrmann (2013) arrival time prediction algorithm, *refmod96*. The goodness-of-fit for a v_p model is estimated using a χ^2 parameter,

$$\chi^2 = \sum_{g=1}^{2} \sum_{h=1}^{N_g} \left(\frac{O_{gh} - C_{gh}}{\varepsilon_g} \right)^2 \tag{S1}$$

where g indicates whether the arrival is the first-arrival at the station ($g = 1$) or a later arriving reflection phase ($g = 2$), and h is an index for the stations observing each type of arrival such that $h = [1, \ldots, N_g]$ and $N_1 = 12, N_2 = 10$. The observations are denoted O_{gh}. Errors, ε_g, for each arrival type have been estimated based on their approximate quarter pulse width, with $\varepsilon_1 = 0.015$ s and $\varepsilon_2 = 0.05$ s.

Our baseline model is identified by minimising χ^2 using a grid search across five parameters: two layer thicknesses (H_2, H_3, where H_1 is fixed as 7 m) and three velocities ($v_{p,2}, v_{p,3}, v_{p,4}$ where $v_{p,1}$ is fixed at 1.18 km/s). The numerical H and v_p subscripts increase sequentially away from the surface; layer 1 is the fixed low-velocity sediment layer, layer 4 is the terminating halfspace.

The 10000 four-layer models resulting in the lowest χ^2 values are illustrated in Fig. S6, with the best fitting model parameters provided in Table 3 of the main paper. The absolute χ^2 values are smaller than the number of observations (22), suggesting that the error terms ($\varepsilon_1, \varepsilon_2$) are conservative estimates. There is a trade-off between velocity and thickness for the layers (Fig. S7). All plausible models (Fig. S6) indicate an increasing v_p with depth. For example, in our preferred (minimum χ^2)

model v_p increases from $v_{p,2} = 1.7$ km/s just below the thin near-surface layer to $v_{p,4} = 4.4$ km/s at a depth of ∼430 m.

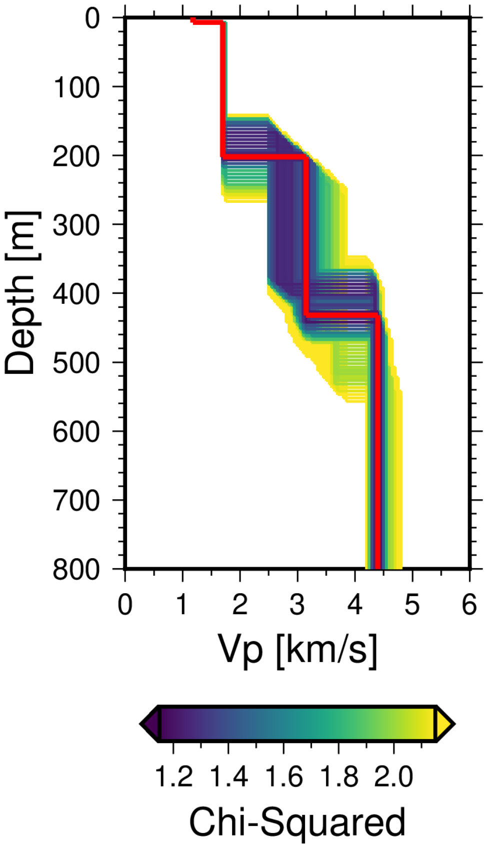

Figure S6: The 10000 v_p models that exhibited the lowest χ^2 values (eq. S1) within the five parameter grid search used to identify our baseline (lowest χ^2) four-layer v_p model (red line). The plotted models represent <0.1% of the considered parameter space.

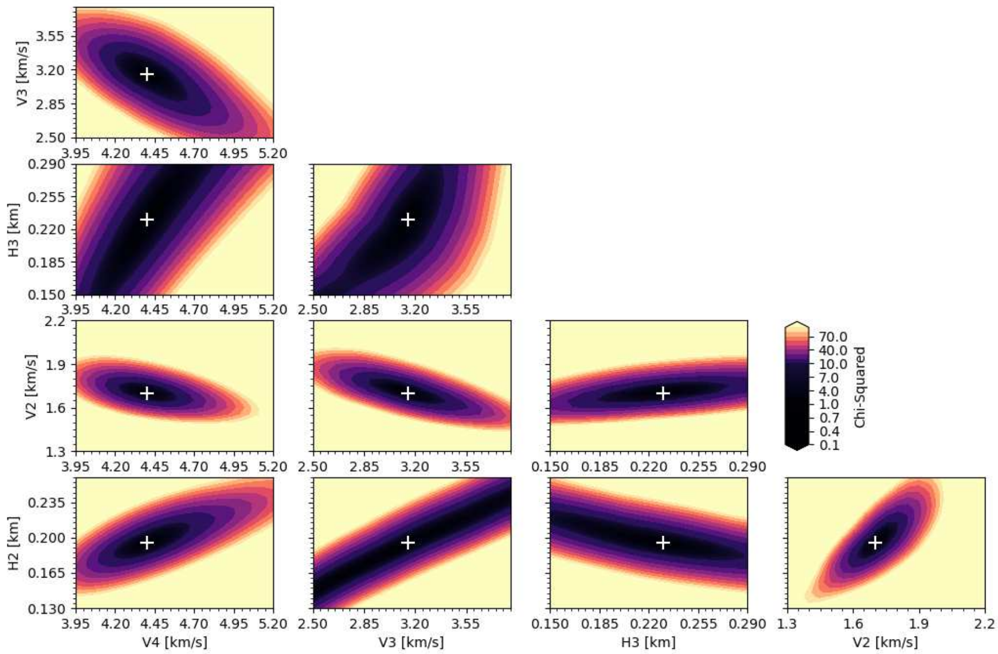

Figure S7: Individual two-dimensional slices through the χ^2 hyperspace for the five parameter grid search to identify the baseline four layer v_p model. The numerical subscripts refer to the layer position in a downwards sense from the surface; layer 1 thickness (H_1) and velocity (v_1) are fixed and so are not shown, layer 4 is a halfspace so H_4 is not a variable.

G A simple Q_p model for the Foulness Subsurface

The numerical waveform modelling undertaken in this study requires, in addition to seismic velocity values, seismic attenuation property estimates for each layer of the input model. The attenuation is characterised by the quality factor, Q. Here we develop a simple depth-dependent *P*-wave quality factor, Q_p, model based on our understanding of the most likely geologic materials beneath Foulness (see for example Section 3, Geological Setting, within the main paper). This Q_p model is employed in the wavenumber integration simulations that underpin the *P*-wave amplitude models (Fig. 7, main paper). Importantly, testing has shown that for the low frequencies (<30 Hz) and relatively short stand-off distances (<7 km) considered in this study, the Q_p structure has little impact upon the synthetic *P*-wave amplitude results. Indeed, models using a constant depth-independent Q_p value of 500 (i.e., a lower attenuation than is anticipated at the trial site) only increase modelled *P*-wave amplitudes by <15%. Moreover, the predicted amplitude variations with distance (Fig. 7, main paper) are insensitive to the Q_p model used.

For the Q_p model (Table S2) we consider four geological units, broadly corresponding to those identified from borehole logs (Section 3, main paper). We take the additional simplifying step of aligning these units with the best-fitting four-layer *P*-wave velocity model constrained using FSCT seismic data (see Section F above). The four layers, and the justification for the corresponding Q_p estimates are:

- Superficial deposits of estuarine and river alluvium. We rely on published work as we have no Foulness-specific data. Experiments on unconsolidated sands, and vertical seismic profile (VSP) measurements on near-surface layers, suggest Q_p values of between 4 and 10 are appropriate (e.g., Mangriotis et al., 2013; Krohn and Murray, 2016; Crane et al., 2018). We choose to use Q_p=5.

- London Clay. Q_p values for the upper clay layers have been determined using refraction data collected during a site survey prior to FSCT (Sindi, 2019). Frequency-dependent Q_p values were estimated using a logarithmic decrement method; at the lowest sampled frequency, 110 Hz, we find Q_p =95±16.

- Cretaceous Chalk. No site-specific Q_p information is available for the Chalk beneath Foulness; we rely on published work. Studies beneath the North Sea have estimated Q_p values of between 100 and 300 within the Chalk (e.g., Prieux et al., 2013; Gamar-Sadat et al., 2016). We choose to use a value of Q_p=150, as the Foulness borehole logs suggest the Chalk may be fractured and soft.

- Gault Clay and Palaeozoic Basement. No site-specific Q_p information is available. Although we acknowledge this value is poorly constrained we use Q_p=200, as results beneath the North Sea (e.g., Gamar-Sadat et al., 2016) do not indicate a large Q_p difference with respect to the overlying chalk.

For completeness we note that the numerical modelling also requires a Q_s value; throughout the paper we have used Q_p/Q_s=1 (e.g., Prasad et al., 2005) although our testing suggests that the simulated *P*-wave amplitudes are insensitive to the choice of Q_s.

Table S2: A simple Q_p model for the sub-surface geology beneath Foulness.

Geology	Q_p	Depth range [m] Baseline four-layer model	Preferred model	Q_p literature
Superficial Deposits	5	[0,7]	[0,7]	Crane et al. (2018) Mangriotis et al. (2013) Krohn and Murray (2016)
London Clay	95	[7,202]	[7,196]	Sindi (2019)
Cretaceous Chalk	150	[202,432]	[196,436]	Gamar-Sadat et al. (2016) Prieux et al (2013)
Gault Clay and Palaeozoic Basement	200	>432	>436	Gamar-Sadat et al. (2016)

H Wavenumber Integration Modelling: Input and Additional Results

H.1 Model inputs

Below we provide an example velocity model input file for the Herrmann (2013) wavenumber integration software. This corresponds to the v_p/v_s gradient model used in Fig. 7c of the main paper.

```
MODEL.985
Model_985
ISOTROPIC
KGS
FLAT EARTH
1-D
CONSTANT VELOCITY
LINE08
LINE09
LINE10
LINE11
H(KM) VP(KM/S) VS(KM/S) RHO(GM/CC) QP QS ETAP ETAS FREFP FREFS
0.007 1.181 0.148 1.406 5 5 0.00 0.00 1.00 1.00
0.025 1.700 0.243 1.755 95 95 0.00 0.00 1.00 1.00
0.025 1.700 0.283 1.755 95 95 0.00 0.00 1.00 1.00
0.055 1.700 0.340 1.755 95 95 0.00 0.00 1.00 1.00
0.042 1.935 0.484 1.876 95 95 0.00 0.00 1.00 1.00
0.042 2.170 1.085 1.978 95 95 0.00 0.00 1.00 1.00
0.042 2.406 1.203 2.063 150 150 0.00 0.00 1.00 1.00
0.018 2.641 1.321 2.135 150 150 0.00 0.00 1.00 1.00
```

```
0.018 2.876 1.438 2.196 150 150 0.00 0.00 1.00 1.00
0.152 3.268 1.634 2.279 150 150 0.00 0.00 1.00 1.00
0.000 3.268 1.634 2.279 200 200 0.00 0.00 1.00 1.00
```

For the source pulse within the Herrmann (2013) `hpulse96` program, we use a parabolic pulse with a base width of 0.064 s, and return velocity seismograms such that the displacement amplitude can be measured using the same methodology as that utilised for the data (see Section 4.4, main paper).

An example of the Herrmann (2013) workflow to generate a synthetic seismogram is shown below. Refer to the Herrmann (2013) program suite manual for details:

```
hprep96 -HR 0 -HS 0.00232 -M Model.d -d foulness_distance.txt -EQEX
hspec96
hpulse96 -V -p -l 4  > hpulse96.out
fmech96 -E -M0 3.0e18 -A 0.0 -B 180.0 < hpulse96.out > file96.out
f96tosac -B < file96.out
```

where the model file, `Model.d`, is of the form shown above, and the distance file, `foulness_distance.txt`, provides information on where the model sensors are located. Again, see the Herrmann (2013) program suite manual for details.

H.2 Supplementary Results Supporting High v_p/v_s Ratio Sediment Interpretation

The key numerical modelling results are shown in Fig. 7 of the main paper. In Fig. S8 we provide results from one extra model. This utilises the same v_p structure as that in the v_p/v_s gradient model of Fig. 7c (main paper) but employs a constant v_p/v_s of 2.00 throughout. Similar to the results shown for simpler velocity structures in Figs. 7a and 7b (main paper), the observed *P*-wave arrival amplitudes cannot be reproduced without the high v_p/v_s in the upper sediment layers.

Record sections of the simulated waveforms, aligned using a reduced time transformation, assist with understanding why high v_p/v_s ratios are required (Fig. S9). In the following description, numbers in square brackets (e.g., [1]) refer to the annotations in Fig. S9. At short source-to-receiver distances (<400 m) the *P*-wave displacements in the [0.5,5] Hz passband are reduced for the v_p/v_s=2 case [1] due to interference with the *S*-wave arrival; when the upper sediments have $v_p/v_s \gg 2$ a significantly larger *P*-wave is simulated [4], consistent with the observations (e.g., Fig. 7c, main paper).

Increased v_p/v_s ratios in the model velocity profiles also result in larger, and less rapid decay of, refracted arrival amplitudes at distances >800 m; compare [2] and [5] for arrivals in the [0.5,5] Hz passband, with similar results observed at [3,30] Hz. The only difference in the underlying velocity models are the varying v_p/v_s ratios in the upper 150 m of sediment. Therefore, the amplitude difference is likely due to increased trapping of energy within the upper 150 m for the model where the layers exhibit a higher (*S*-wave) impedance contrast with the layers beneath (i.e., Fig. 7c, main paper).

In the higher [3,30] Hz frequency band, the enhancement of the *P*-wave amplitudes at distances of between ~650 and 1000 m is apparent regardless of the v_p/v_s regime ([3] and [7]). This appears to be due to constructive interference of the direct wave and a refracted wave from a depth of ~150 m, consistent with finite-difference simulations showing the merging of the two arrivals (Fig. S10d to f). The amplitude increase, relative to the direct wave amplitude, occurs over a narrow distance range for the v_p/v_s=2 case [3] when compared to the $v_p/v_s \gg 2$ case [7]. The wider distance range over which the amplitudes are enhanced [7], and the elevated refraction amplitudes [8], for the $v_p/v_s \gg 2$ case are consistent with the observations (Fig. 7c, main paper).

At the higher frequencies it is easier to observe later arriving phases generated by reflections in the $v_p/v_s \gg 2$ case ([6] and [9]), compared to the v_p/v_s=2 case (Fig. S9b). At distances <700 m [6] these reflections are consistent with finite-difference modelling results that exhibit multiple reverberations within the upper layers of the velocity model (e.g., Fig. S10c). At distances >900 m the dominant late arriving phase [9] tends towards a velocity consistent with a horizontally propagating

P-wave through the upper sediment. Such a phase is the largest observed seismic phase at distances >1000 m for the FSCT shots (see Fig. 5, main paper).

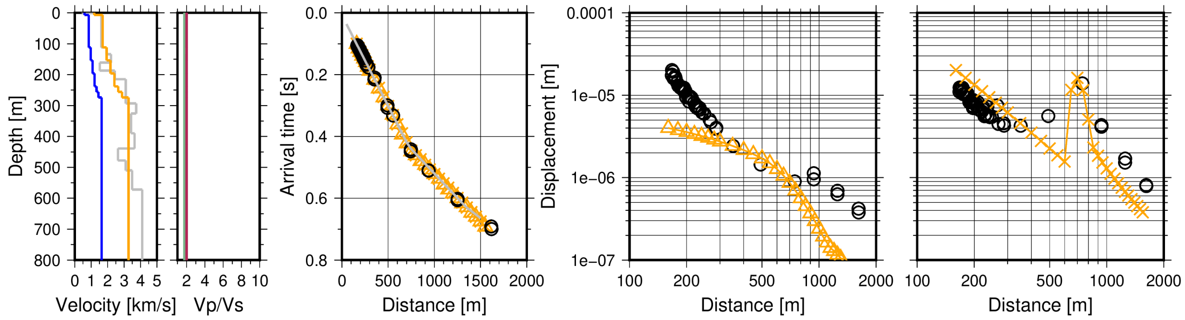

Figure S8: A comparison of arrival time and displacement amplitude observations with numerical modelling results for a simplified seismic velocity model. The model is identical to the preferred model (Fig. 7c, main paper) except that the v_p/v_s ratio is kept constant at 2.00. From left to right the five panels for each model give (i) the model v_p and v_s profiles (in orange and blue respectively) in comparison to the v_p profile estimated by Can (2020) (in grey), (ii) the model v_p/v_s ratio (in maroon) in comparison to a v_p/v_s ratio of 1.73 (in green), (iii) a comparison of the observed and modelled *P*-wave arrival times, and comparisons of the initial *P*-wave amplitudes in comparison to observations for explosion S2 in the (iv) [0.5,5]Hz and (v) [3,30]Hz passbands.

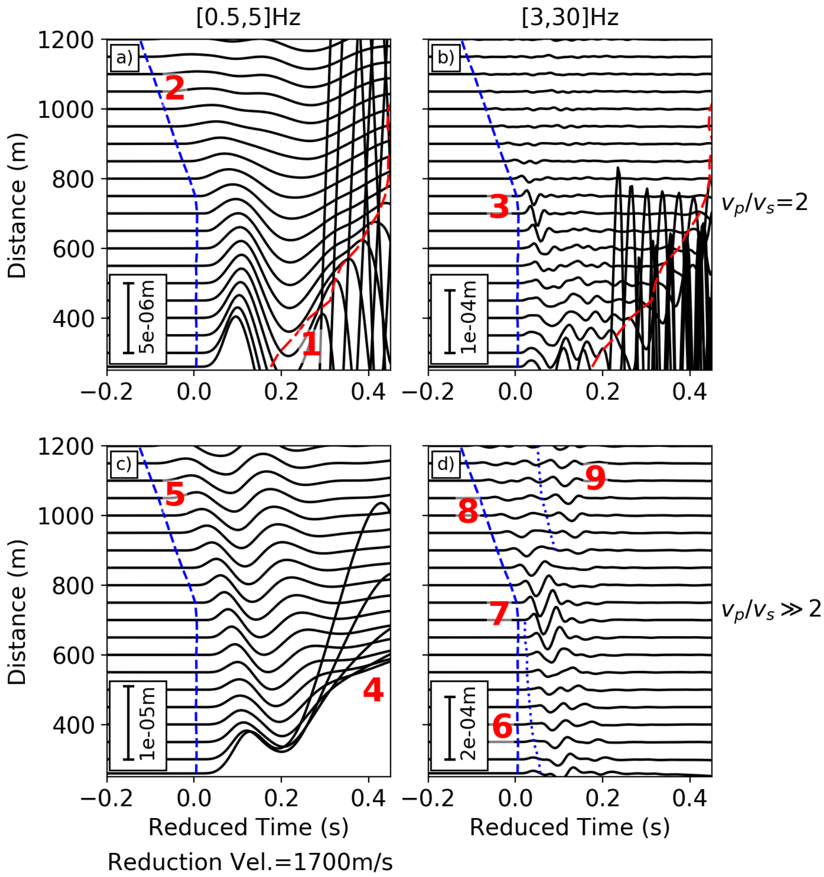

Figure S9: Simulated displacement waveforms resulting from wavenumber integration modelling for the model employing a v_p/v_s ratio of 2 (panels a and b; see Fig. S8 for model description) compared to our final model that incorporates higher v_p/v_s ratios in the upper layers (panels c and d; see Fig. 7c, main paper). *P*- and *S*-wave arrival times picked from unfiltered synthetic seismograms are shown by blue and red dashed lines, respectively. The *S*-wave arrives at later times than shown for the model in panels c and d. Blue dotted lines in panel d indicate later arriving reflections. Red numbers refer to nine features described in the accompanying text. The reduced time is calculated as (time − (source-to-receiver distance / reduction velocity)).

I Wavefield Snapshots From a Finite Difference Simulation

To provide a visualisation of the evolving seismic wavefield as it propagates through our preferred Foulness subsurface model (e.g., Fig. 7c, main paper), we employed the 3-D seismic wave propagation package SW4 (Petersson et al., 2023), a time-domain fourth-order accurate in space and time finite-difference code, based on the summation by parts principle (Petersson and Sjogreen, 2012). The code solves the seismic wave equations (elastic or visco-elastic) in Cartesian coordinates, and so is well suited to local propagation simulations. We focus our simulation on the distances associated with the observed *P*-wave amplitude increases (700 to 1000m from the source, Fig. 7 of the main paper), therefore our model domain is limited to x=700m, y=1400m, z=1000m (x, y are horizontal dimensions, z is the vertical dimension) and we focus upon propagation in the y-z plane. We discretized the domain with a grid spacing of 1 m allowing us to resolve frequencies up to 70 Hz for *P*-waves and 10 Hz for *S*-waves with 15 points per minimum wavelength. For the source we used an explosion (isotropic moment tensor with moment 1×10^{10} N·m) and a Gaussian wavelet for the source time function. We focus our simulation efforts on shot S2; the source was placed at x=350m, y=400m and z=2.32m (i.e., 2.32m below the ground surface) within our model domain. SW4 is capable of incorporating realistic topography by using a curvilinear mesh near the free surface to honour the free surface boundary condition. However, the topographic variation across Foulness Island is minimal and therefore topography was not included in the simulations. Boundary conditions included a free surface condition on the top boundary, and non-reflecting far-field boundary conditions on the other boundaries.

Within the simulation the wavefield initially propagates hemispherically outward from the source (Fig. S10a), but interactions with seismic velocity contrasts at depths of between 110 and 275 m distort the wavefield by generating reflections, refractions and *P*-to-*S* conversions (Fig. S10b). By ~0.35 s after the detonation (Fig. S10c) the surface wavefield (at distances of between 350 and 400 m from the explosion) is composed of a superposition of waves reflected at depth and the direct *P*-wave propagating horizontally away from the source. As time progresses more arrivals, generated at deeper interfaces and propagating at steeper angles with respect to the ground surface, coalesce into the first arriving P-wave phase (Fig. S10d to f). At 0.55 s after the explosion (Fig. S10f) there appears to be a focusing of energy at the ground surface $\sim$700 m from the source. Beyond this point (and at later times) the surface wavefield appears to become more spread laterally and the vertical surface displacements begin to decrease (Fig. S10g). This visualisation of the wavefield is consistent with the results of the wavenumber integration modelling detailed in Section 5 of the main paper.

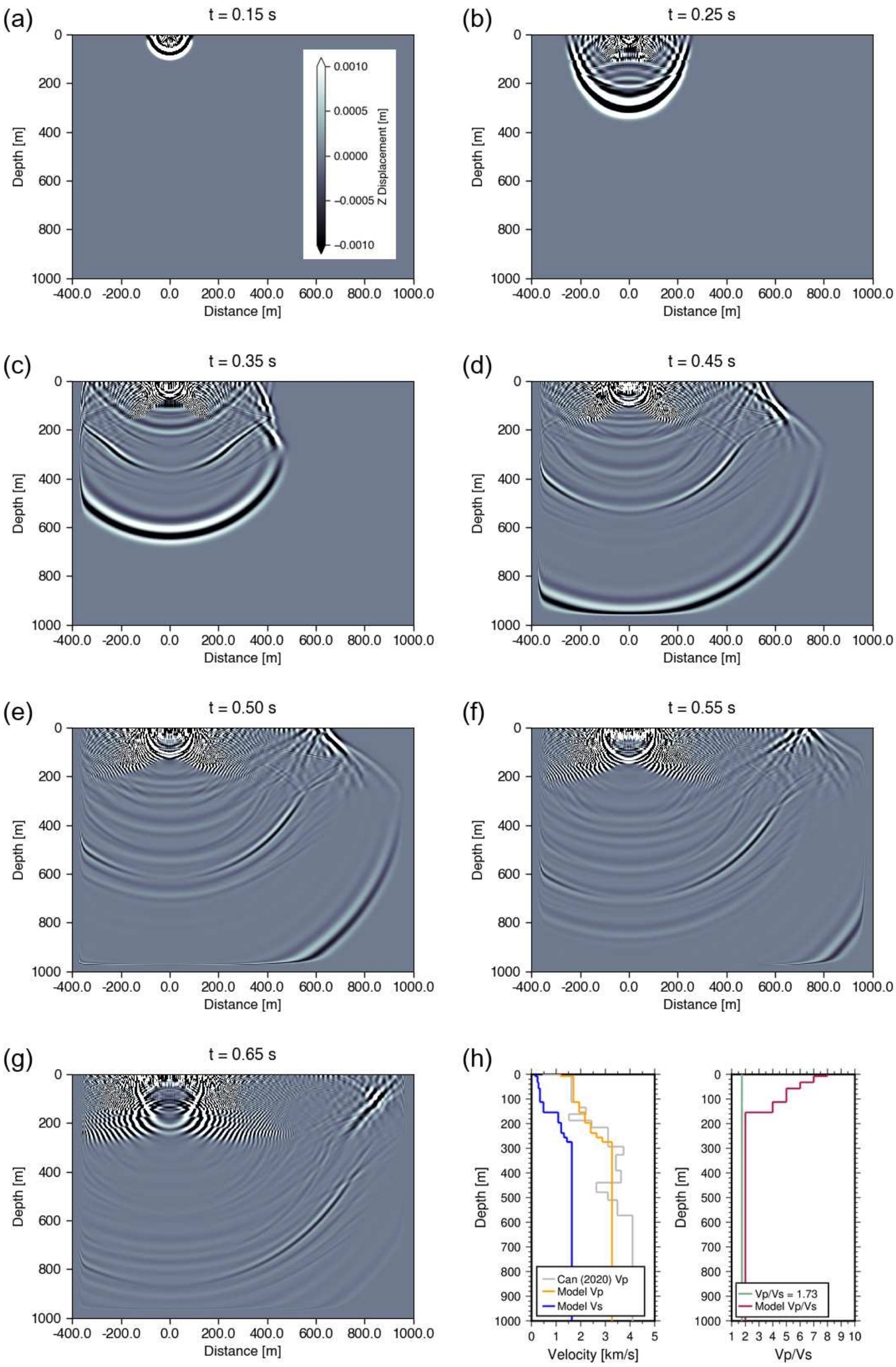

Figure S10: Snapshots from SW4 finite-difference simulations (panels a to g) showing the evolution of the vertical component seismic displacement wavefield when propagated through our preferred model.

J β values, and covariance: 3 to 30 Hz passband

Displacement model parameters for the [0.5,5] Hz passband (for comparison with Ford et al., 2021) are given in Table 4 and 5 of the main paper. Here, corresponding parameter tables are provided for the [3,30] Hz passband. Fig. S11 provides a comparison of the model predictions and the data within the [3,30] Hz passband, for comparison with Fig. 8 in the main paper.

Table S3: Least-squares estimates of the *P*-wave displacement model parameters (β_n, where $n = 1, \ldots, 5$, eq. 5, main paper) and the associated covariance matrix, for observations in the [3,30] Hz passband and the [150,300] m source-to-receiver distance range.

Parameter		β_1	β_2	β_3	β_4	β_5
Mean Value		-4.05	-2.22	-4.07	4.16	0.71
Covariance	β_1	0.027	-0.0051	-0.015	-0.027	-0.0052
	β_2	-0.0051	0.0010	0.0025	0.0045	0.00089
	β_3	-0.015	0.0025	0.016	0.025	0.0070
	β_4	-0.027	0.0045	0.025	0.044	0.011
	β_5	-0.0052	0.00089	0.0070	0.011	0.0041

Table S4: Least-squares estimates of the *P*-wave displacement model parameters (β_m, where $m = 1, 2$, eq. 5, main paper) and the associated covariance matrix, for observations in the [3,30] Hz passband and the [1000,7000] m source-to-receiver distance range. β_p, where $p = 3, 4, 5$, are assumed to take the same values as the inversion undertaken at closer source-to-receiver distances (Table S3).

Parameter		β_1	β_2
Mean Value		-3.47	-1.91
Covariance	β_1	1.0	-0.16
	β_2	-0.16	0.026

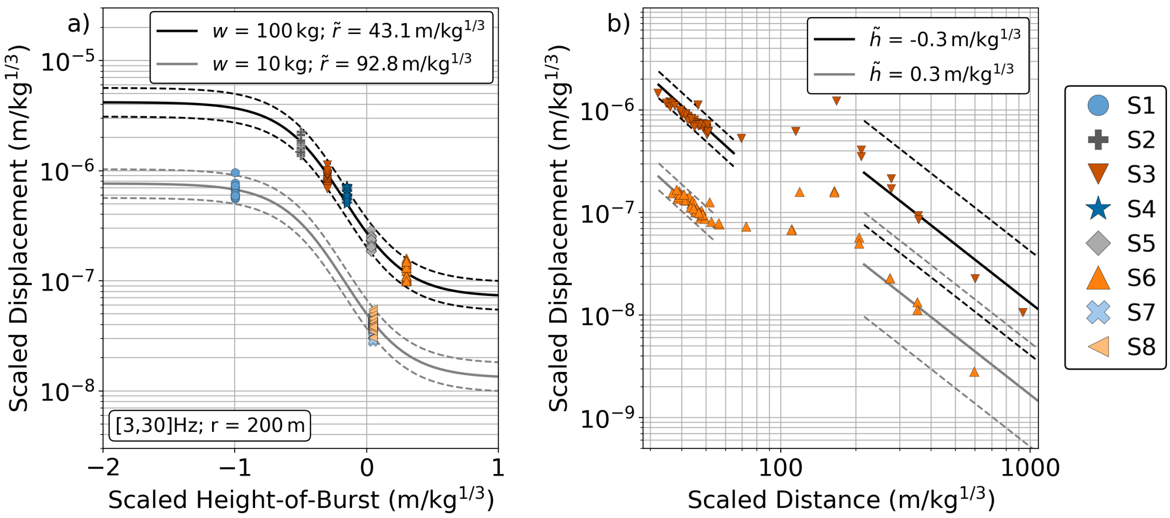

Figure S11: The scaled seismic displacement model (eq. 5, main paper) fit to the measured FSCT amplitudes in the [3,30]Hz passband, as a function of scaled HoB (panel a) and scaled distance (panel b). Variations with HoB (panel a) are shown at r=200 m, within a distance range for which there is a high density of geophone recordings (Fig. 1b, main paper). The superimposed measured amplitudes (coloured symbols) are taken from the [180, 220] m distance range. Two models are shown, corresponding to the scaled distances of the 100 kg shots (black lines) and the 10 kg shots (grey lines). The solid lines are the mean model, with the dashed lines representing the 95% prediction intervals. Variations with scaled distance (panel b) are shown for a below ground explosion (S3, $\tilde{h}$=−0.3 m/kg$^{1/3}$) and an above ground explosion (S6, $\tilde{h}$=0.3 m/kg$^{1/3}$); the models are only shown across the scaled distances for which they were calculated.